β-delayed neutron-emission and fission calculations within relativistic quasiparticle random-phase approximation and a statistical model

Minato, Futoshi; Marketin, Tomislav; Paar, Nils

Source / Izvornik: **Physical Review C, 2021, 104**

Journal article, Published version
Rad u časopisu, Objavljena verzija rada (izdavačev PDF)

https://doi.org/10.1103/PhysRevC.104.044321

β-delayed neutron-emission and fission calculations within relativistic quasiparticle random-phase approximation and a statistical model

Futoshi Minato ,[1,*] Tomislav Marketin ,[2] and Nils Paar[2]

[1]*Nuclear Data Center, Japan Atomic Energy Agency, Tokai, Ibaraki 319-1195, Japan*

[2]*Department of Physics, Faculty of Science, University of Zagreb, 10000 Zagreb, Croatia*

(Received 23 February 2021; revised 21 July 2021; accepted 23 September 2021; published 19 October 2021)

Background: β-delayed neutron emission and fission are essential in r-process nucleosynthesis. Although the number of experimental studies covering r-process nuclei has recently increased, the uncertainties of β-delayed neutron emission and fission are still large for r-process simulations.

Purpose: Our aim is to introduce a theoretical framework for the description of β-delayed neutron-emission and fission rates based on relativistic nuclear energy density-functional and statistical models and investigate their properties throughout the nuclide map.

Methods: To obtain β strength functions, the relativistic proton-neutron quasiparticle random-phase approximation is employed. Particle evaporations and fission from highly excited nuclear states are estimated by the Hauser-Feshbach statistical model. β-delayed neutron branching ratios P_n are calculated and compared with experimental data, and the β-delayed fission branching ratio P_f are also assessed by using different fission barrier data.

Results: Calculated P_n are in a good agreement with the experimental data and the root mean square deviation is comparable to results of preceding works. It is found that energy withdrawal by β-delayed neutron-emission sensitivity varies P_n, especially for nuclei near the neutron drip line. P_f depend sensitively on fission barrier data. It is found that not only the barrier height but also the number of barrier humps is important to evaluate P_f.

Conclusions: The framework introduced in this work provides an improved theoretical description of the β-delayed neutron emission and fission. Since P_f as well as P_n depend strongly on fission barrier information, four kinds of fission barrier data are used in this work to allow further sensitivity studies of the r-process nucleosynthesis on the nuclear fission. More studies on fission barrier are highly requested to assess the role of β-delayed fission in the r-process study. A complete set of calculated data for β-delayed neutron emission and fission are summarized as a table in supplemental material for its use in r-process studies as well as to complement a part of nuclear data in which no experimental data are available.

DOI: 10.1103/PhysRevC.104.044321

I. INTRODUCTION

The origin of chemical elements in the universe is the long-standing problem and one of the hottest topics in astrophysics. Our knowledge accumulated so far indicates that heavy elements in nature are generated by the dynamical processes of stars. In particular, about a half of the elements heavier than iron is considered to be produced by the r process [1,2] (the other half is by the s process [1]). Although it is still not concluded where the r process occurs, recent studies employing observation of gravitational waves provide evidence that a neutron-star merger is one of the possible sites of the r process [3,4].

The solar r-process abundance pattern shows a characteristic mass distribution that has three peaks around $A = 80$–90, 130–138, and 195–208 [5–7]. The r-process simulation suggests that the origin of these peaks is related to neutron magic numbers of $N = 50$, 82, and 126, which is also related to nuclear mass [5,6,8]. However, the peak positions and abundance ratios cannot be reproduced only by considering the nuclear mass effects. Neutron capture, β decay, and other decay modes sensitively influence the abundance pattern of the r process [6,9–27].

During the r process, β^- decay (hereinafter, we simply call it β decay) increases the atomic number of nuclei and produces daughter nuclei in a highly excited state. Depending on the excitation energy, the daughter nuclei decay through several particle-emission channels. In particular, β-delayed neutron emission and fission (hereinafter we call them BDNE and BDF, respectively) play a subsidiary role in the r-process abundance. BDNE produces two different effects on the r-process abundance. The first is that it leads nuclei in an r-process site to detour the β^--decay path $(A, Z) \rightarrow (A, Z+1)$ by reducing their neutron number, for example, $(A, Z) \rightarrow (A-1, Z+1)$ in case of one-neutron ($1n$) emission, where Z equals the proton number. This effect smooths the even-odd fluctuation in the final r-process abundance pattern [19–21]. Another effect of BDNE is that it feeds neutrons to the r-process environment. This effect

*minato.futoshi@jaea.go.jp

retards the progress of the freeze-out for the "cold" r-process scenario [6].

The role of BDF is to reduce the abundance of heavy elements by breaking daughter nuclei into two or more fragments during the r process and its freeze-out phase. Furthermore, the fission fragments restart to capture environmental neutrons and grow up toward heavy elements again. This phenomena, also known as fission recycling, affects a wide range of the r-process abundances together with neutron-induced fission [22–27]. An understanding of fission in the r-process is essential to answer the naive question, are superheavy elements produced by dynamical processes in stars [28]?

A lot of experimental measurements of BDNE have been carried out because of its importance in applications to the r-process as well as for nuclear data evaluation (e.g., see Refs. [29–33] for recent works). However, the experimental difficulty rapidly increases as one tries to study very-neutron-rich nuclei because of the low statistics. For this reason, there are still nuclei for which BDNE and BDF have not been measured yet. In particular, for BDF, only seven cases are recognized near the β-stability line [34] (see Ref. [35], which summarizes experimental studies for BDF).

Nuclei that are not investigated by experiment have to be covered by theoretical models. Empirical systematics is a useful approach and is provided in, e.g., Refs. [36–39] for the β-delayed neutron branching ratio P_n and even for BDF in Refs. [35,40]. Gross Theory (GT2) [41,42] is also an effective tool. It has provided β strength functions systematically for nuclei in the nuclear chart, and not only half-lives but also P_n and the β-delayed fission branching ratio P_f have been calculated [20]. However, it is not clear whether a phenomenological approach based on the GT2 is valid for very-neutron-rich nuclei.

Another effective approach for theoretically predicting P_n and P_f is a microscopic model. Typical approaches are the configuration interaction (CI) model, the quasiparticle random-phase approximation (QRPA), and the finite amplitude method (FAM), which is essentially the same as the QRPA but solves the problem in a different way. Recently, the interacting boson model (IBM) based on the mean-field approach has been applied to β-decay calculations as well [43]. Although CI models are actively applied to the calculation of half-lives for r-process nuclei around $N = 50$, 82, and 126 shell closures, the application is still restricted to limited nuclei due to the increasing computational cost [14,44,45]. For this reason, to calculate β decay for r-process nuclei, the QRPA [46–51] and FAM [52–54] are applied in practice.

One of us has calculated P_n systematically for neutron-rich nuclei in the framework of the proton-neutron relativistic quasiparticle random-phase approximation (pn-RQRPA) [15]. This microscopic model starts from an effective interaction determined by experimentally known ground-state properties of nuclei and is believed to provide a more reliable β strength function than purely phenomenological approaches. To predict β-delayed neutron branching ratios, a simplified approach (hereinafter referred to as the cutoff method) assuming that nuclei with excitation energies above the neutron threshold always emit β-delayed neutron has been used, as done in Refs. [48–50]. This assumption corresponds with a picture that neutron emission is the only exit channel above neutron thresholds and the kinetic energy of β-delayed neutrons is zero. This prescription clearly omits the nuclear structure, the selection rule of the decay chain, competition with other decay channels, and kinematics. In fact, it is pointed out in Ref. [55] that a competition between neutron emission and γ deexcitation gives a non-negligible variation to the calculation for P_n of nuclei, especially near the neutron drip line.

One of the approaches to treat nuclear decay in a more physical and complete way is to apply a statistical decay model, for example, the Hauser-Feshbach statistical model (HFM) [56]. The HFM considers nuclear structure effects through level densities and selection rules of the decay chain, competition with other decay channels, and kinematics that the cutoff method omitted. Combination of the QRPA β strength function and the statistical decay model is therefore a feasible approach and has been carried out by several groups using FRDM + QRPA [26,57,58] and nonrelativistic QRPA [46,47,51,59–61]. The aim of this paper is directed at estimating P_n and P_f by using this approach, namely, by combining pn-RQRPA and HFM. Hereinafter, we refer to the present work as pn-RQRPA + HFM to distinguish it from the preceding work of pn-RQRPA [15].

This paper is organized as follows: In Sec. II, we describe theoretical framework to calculate BDNE and BDF using pn-RQRPA + HFM. In Sec. III, the results obtained in this work are presented and discussed in comparison with experimental data and preceding works. Section IV summarizes this work and presents some perspectives. The complete data table containing the BDNE and BDF branching ratios is available in the Supplemental Material [62].

II. THEORETICAL FRAMEWORK OF *pn*-RQRPA + HFM

A. β-delayed neutron and fission branching ratios

Our calculation is composed of two parts: First, we prepare β strength functions for the Gamow-Teller (GT) and the first-forbidden (FF) transitions by using the pn-RQRPA [15]. As second step, we carry out the calculation of statistical decay from the compound state by using the HFM calculation with excitation energy and spin-parity given by the pn-RQRPA. P_n and P_f are then obtained by multiplying neutron and fission emission probabilities by the β-decay rates, respectively.

A fully self-consistent covariant density-functional theory (CDFT) is adopted in this work. The ground state of all nuclei is calculated with the relativistic Hartree-Bogoliubov (RHB) model with the D3C* interaction [63]. The ground state of odd nuclei are computed by employing the same model as that of even-even nuclei, namely, we impose the expectation value of the particle number operator to be an odd proton and/or neutron number. On the top of the RHB model, excited states are obtained within the pn-RQRPA. More details about the pn-RQRPA used in this work are given in Ref. [15].

We assume that daughter nuclei reach the compound state, namely, the thermally equilibrium state, soon after the β decay. In the compound state, daughter nuclei lose their initial information that they had before the β decay, except for the spin-parity and the total energy of the system. The number of protons and neutrons of the initial nuclei (precursor) are defined as Z and N, respectively. Accordingly, the number of protons and neutrons of the daughter nuclei are given by $Z+1$ and $N-1$, respectively.

The HFM calculation is executed with various different excitation energies and spin-parity states of daughter nuclei. However, excitation energies $E_{i,\mathrm{QRPA}}$ computed from the *pn*-RQRPA are not identical to those of daughter nuclei. We thus need some transformations. In the framework of *pn*-RQRPA, coherent proton-neutron two-quasiparticle configurations are regarded as excited states, where the lowest state becomes the ground state of the daughter nuclei. Namely, the excitation energies of the *pn*-RQRPA has to be subtracted from the lowest value to obtain those with respect to the daughter nuclei. However, it is time consuming and not straightforward to find the lowest state within the pn-RQRPA. As an alternative method to connect the *pn*-RQRPA and the HFM calculations, we use in this work the noninteracting quasiparticle approximation, in which an odd-mass nucleus is approximated by one quasiparticle state plus the wave function of the neighboring even-mass nucleus. Based on this approximation, the excitation energies with respect to daughter nuclei are computed through [64,65]

$$E_i^* = E_{i,\mathrm{QRPA}} - E_{\mathrm{corr}}, \tag{1}$$

$$E_{\mathrm{corr}} = \begin{cases} E_{p_0} + E_{n_0} & (\beta \text{ decay for even-even nucleus}) \\ E_{p_0} & (\text{for even-odd}) \\ E_{n_0} & (\text{for odd-even}) \\ 0 & (\text{for odd-odd}), \end{cases} \tag{2}$$

where the index i denotes an excited state of the daughter nuclei with spin-parity J^π, and E_{p_0} and E_{n_0} are the lowest quasiparticle energies of proton and neutron calculated from the RHB, respectively.

We should mention one issue arising from the use of the noninteracting quasiparticle approximation in Eq. (1). The *pn*-QRPA excitation energies $E_{i,\mathrm{QRPA}}$ consider correlations caused by the two-body residual interactions, while the lowest quasiparticle energies in Eq. (2) does not. As a result, $E_{i,\mathrm{QRPA}}$ is frequently lower than E_{corr}, and E_i^* becomes negative for some nuclei. Although negative excitation energies are physically incorrect, we adopt an approximation that the HFM calculation with $E_i^* < 0$ MeV ends up with no evaporation from nuclei and the corresponding states become the ground state.

Carrying out the HFM calculation, we obtain production ratios of evaporation residues with proton number $Z' = Z+1$ and neutron number $N' = N-1-x$ defined as $p_{xn}^{(n)}(E_i^*)$, and spectra of emitted particles defined as $d_\nu(E_\nu, E_i^*)$. Here, E_ν is the kinetic energy of the outgoing particle and $\nu = \{n, \gamma, p, \alpha\}$ represents a kind of the emitted particle, where the letters in the brackets represent neutron, γ ray, proton, and α particle, respectively. We did not consider other light-particle emissions d, t, and ^{3}He because they are strongly hindered for the neutron-rich nuclei of interest. For heavy nuclei, the fission channel, i.e., BDF, is open. BDF occurs directly after β^- decay of parent nuclei, i.e., (β^-, f), or indirectly after multineutron emissions following the β decay, i.e., (β^-, xnf). The fission probabilities from an excited state i are defined as $p_{xn}^{(f)}(E_i^*)$. The case of $x=0$ means fission occurs directly from the daughter nucleus with no neutron emission. The functions of $p_{xn}^{(n)}(E_i^*)$, $p_{xn}^{(f)}(E_i^*)$, and $d_\nu(E_\nu, E_i^*)$ are computed by the HFM calculation implemented in the CCONE code [66]. Although we do not go into details about the HFM because the formalism is given in, e.g., Refs. [55,60,66], we will explain the nuclear input details used in our calculation in the Sec. II B.

The BDNE and BDF branching ratios are calculated by

$$P_n = \sum_x P_{xn} = \frac{1}{R} \sum_{i,x} r_i \, p_{xn}^{(n)}(E_i^*) \tag{3}$$

and

$$P_f = \sum_x P_{xn,f} = \frac{1}{R} \sum_{i,x} r_i \, p_{xn}^{(f)}(E_i^*), \tag{4}$$

respectively, where r_i is the partial β^--decay rates to excited state i calculated by the *pn*-RQRPA, and $R = \sum_i r_i$. β-delayed α (p) emission branching ratios P_α and $P_{xn\alpha}$ (P_p and P_{xnp}) are calculated in the same way. In this framework, the following relations hold:

$$P_n + P_f + P_\alpha + P_p = 1. \tag{5}$$

The BDNE spectrum is calculated by

$$D_n(E_n) = \mathcal{N}_s \sum_i r_i \, d_n(E_n, E_i^*), \tag{6}$$

where $\mathcal{N}_s$ is the normalization factor for spectra to be determined so as to satisfy

$$\int_0^\infty D_n(E_n)\, dE_n = 1. \tag{7}$$

The summation of i of Eqs. (3), (4), and (6) is carried out for $E_i^* \leqslant Q_\beta$. The β-decay Q value is calculated from $Q_\beta = M_{n\mathrm{H}} + \lambda_n - \lambda_p - E_{\mathrm{corr}}$ [15] where $M_{n\mathrm{H}}$, λ_n, and λ_p are the mass difference between neutron and hydrogen atom, and the neutron and proton Fermi energies, respectively.

B. Nuclear input details for Hauser-Feshbach statistical model

1. *β strength function*

The present RHB model is solved by using the D3C* interaction, resulting in discrete quasiparticle states obtained in the canonical basis [63]. The *pn*-RQRPA equation is solved by assuming coherent two quasiparticle (2qp) excitations. In this scheme, the excited states are also discrete. Accordingly, the β strength function also has a discrete shape in terms of excitation energy. However, it is considered that actual excited states have a broad distribution with a width because of coupling to higher-order configurations (4qp, ..., *n*qp excitations) [67] and continuum states, which are not taken into account in the present *pn*-RQRPA. To account for those influences, we introduce a weight function to the β strength functions. We consider two types of weight functions, that is, the Gaussian type and the Lorentzian type:

$$W_w(E) = \begin{cases} \sum_{i\in w} g_J^w \, r_i \frac{1}{\sqrt{2\pi}\Gamma} e^{-\frac{(E-E_i^*)^2}{2\Gamma^2}} & (8) \\ \sum_{i\in w} \mathcal{N}_i \, g_J^w r_i \frac{1}{\pi} \frac{\Gamma/2}{(E-E_i^*)^2 + (\Gamma/2)^2}. & (9) \end{cases}$$

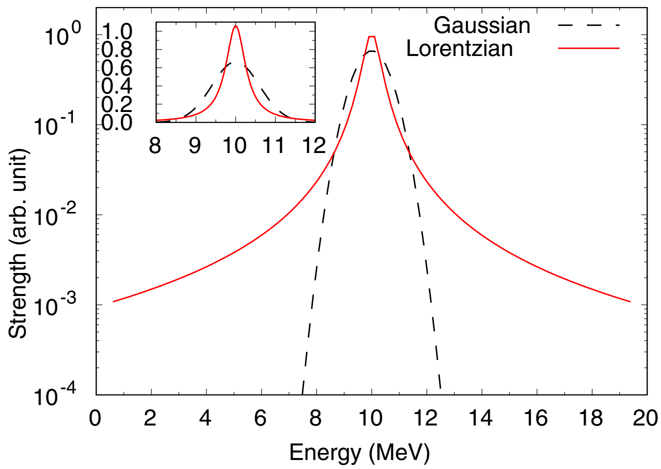

FIG. 1. Weight functions of Gaussian type (the dotted line) of Eq. (8) and Lorentzian (the solid line) type of Eq. (9) with $E^* = 10$ MeV and width $\Gamma = 0.6$ MeV. The inserted panel is depicted in a linear scale

The index w is used to distinguish the GT ($\Delta J^\pi = 1^+$) and the FF transitions ($\Delta J^\pi = 0^-, 1^-, 2^-$), and the factor g_J^w is a statistical factor that will be explained later. Since the Lorentzian function that is proportional to $1/E^2$ has a finite strength even far from the mean, we introduce a cutoff energy $E_{\rm cut}$ to reduce anomalously large strengths at distant energies. This cutoff energy is determined by $L_\omega(E_{\rm cut}) = L_\omega(E_i^*)/1000$, and the weight function of Eq. (9) is active within the energy range of $E_i^* \pm E_{\rm cut}$. The factor $\mathcal{N}_i$ in Eq. (9) is then introduced to renormalize the Lorentzian function to unity. In this scheme, a part of the β strength functions may stray to the negative energies in terms of daughter nuclei. In this case, we integrate the β strengths at negative energies and set them at $E^* = 0$ MeV, namely, the ground state of the daughter nuclei. A schematic picture that depicts Eqs. (8) and (9) with $r = 1$, $E^* = 10$ MeV, and $\Gamma = 0.6$ MeV ($E_{\rm cut} = 9.5$ MeV) are shown in Fig. 1. Within $E^* \pm 2\Gamma$, the Gaussian function has a broader distribution than the Lorentzian function. Beyond this energy range, the Gaussian function rapidly fades out while the Lorentzian function still has a finite strength distribution.

From Eqs. (8) and (9), Eqs. (3), (4), and (6) are rewritten as

$$P_{xn} = \frac{1}{R}\int_0^{Q_\beta} W_w(E) p_{xn}^{(n)}(E) dE, \qquad (10)$$

$$P_{xf} = \frac{1}{R}\int_0^{Q_\beta} W_w(E) p_{xn}^{(f)}(E) dE, \qquad (11)$$

$$D_n(E_n) = \mathcal{N}\int_0^{Q_\beta} W_w(E) d_n(E_n, E) dE, \qquad (12)$$

respectively. In the later section, we determine the width parameter Γ that minimizes the root mean square deviation of P_n from the experimental data.

2. Spin and parity

In case of even-even nuclei, the spin-parity of the ground state is always 0^+ and that of the daughter nuclei is uniquely determined according to the decay types. In case of odd mass nuclei, the situation becomes complicated a little because the spin of the ground state is not always zero and the angular-momentum coupling is relevant to estimate the spin-parity of daughter nuclei. In this work, we use the following method for odd-mass nuclei. First we determine the spin-parity of the ground state of parent nuclei. We adopt the experimental data if they are available. If not, we use the spin-parity of the state with the lowest quasiparticle energy deduced from the RHB calculation, namely, $J_{gs} = j_p$ with $\pi_{gs} = (-)^{l_p}$ and $J_{gs} = j_n$ with $\pi_{gs} = (-)^{l_n}$ for odd-even and even-odd nuclei, respectively. Here, j_p (j_n) and l_p (l_n) are the total and orbital angular momentum of the proton (neutron), respectively. For the spin state of odd-odd nuclei, we apply the Nordheim method [68], which is given by

$$\begin{aligned} J_{gs} &= j_p + j_n \quad \text{if} \quad j_p = l_p \pm \tfrac{1}{2} \quad \text{and} \quad j_n = l_n \pm \tfrac{1}{2}, \\ J_{gs} &= |j_p - j_n| \quad \text{if} \quad j_p = l_p \pm \tfrac{1}{2} \quad \text{and} \quad j_n = l_n \mp \tfrac{1}{2}, \end{aligned} \qquad (13)$$

and the parity is computed via $\pi_{gs} = \pi_{gs}^{(p)}\pi_{gs}^{(n)} = (-)^{l_p+l_n}$. After determining the spin-parity of parent nuclei in this way, we can conclude that of the daughter nuclei according to the β-decay type. The spin of the daughter nuclei (J_f) thus has $|J_{gs} - \Delta J| \leqslant J_f \leqslant J_{gs} + \Delta J$ and the parity $\pi_f = \pi_{gs}\pi_\alpha$, where $\Delta J = 0, 1, 2$ and $\pi_\alpha = \pm$ depending on the type of β transitions. We assumed the equal distribution of the β strength function for each $J_f^{\pi_f}$ state. The factor g_J^w in Eq. (9) is determined so that total amount of the β strength function is conserved. For example, in the case of a $1^\pm$ transition from a parent nucleus with the $J = 3/2$ (1/2) state, $J_f = 5/2, 3/2, 1/2$ (3/2, 1/2) and $g_{3/2(1/2)}^{1^\pm} = 1/3$ (1/2).

In the HFM calculation, transmission coefficients of nucleons and α particles are calculated by the optical potentials of Koning-Delaroche [69] and Avrigeanu [70], respectively. For nuclear level densities, the Gilbert-Cameron method [71] with the Mengoni-Nakajima parameter [72] is adopted. For γ strength functions, the enhanced generalized Lorentzian function [73] is used. Mass data are taken from the global nuclear mass model [74] and used for calculating neutron separation energies S_{xn}, Q_β, Q_α and so on.

Transmission coefficients for fission are calculated as follows: We assume a double- or triple-humped parabolic barrier with the barrier penetrability for each barrier calculated by the Hill-Wheeler equation [75]. The transmission coefficients are obtained by assuming that the fission process occurs through the transition states above the fission barrier. All transition states were approximated by the level-density formula described above. The transmission coefficient of a single barrier for the state having excitation energy E and spin-parity J^π, $T_i(E, J^\pi)$ is calculated by

$$T_i(E, J^\pi) = \int_0^\infty \frac{\rho_i(\epsilon, J^\pi)}{1 + \exp\left(-2\pi \frac{E - V_i - \epsilon}{\hbar\omega_i}\right)} d\epsilon, \qquad (14)$$

where the subscripts $i = A$, B, and C indicate the inner, middle, and outer barriers, respectively, $\rho_i(\epsilon, J^\pi)$ is the level density at the saddle points, and V_i and $\hbar\omega_i$ represent the height and curvature of the fission barrier, respectively. The transmission coefficients for nuclei with double- and triple-humped barriers are approximated to be $T(E,J^\pi) = T_A T_C (T_A + T_C)$ and $T(E,J^\pi) = T_A T_B T_C/(T_A T_B + T_B T_C + T_C T_A)$, respectively.

Since predicted fission barrier data greatly vary among fission barrier data as we will see, our calculation is carried out using four different fission barriers: HFB-14 [76], the Extended Thomas Fermi plus Strutinsky Integral (ETFSI) method [77], the FRDM [78], and the Spherical Basis Method (SBM) [79]. The former two provide multihumped fission barrier data, while the latter two give only single-barrier information. Fission barrier heights of FRDM are relatively low, while those of SBM are relatively high. The curvature parameter we used is $\hbar\omega_A(\hbar\omega_B) = 1.04(0.60), 0.80(0.52), 0.65(0.45)$ MeV for even-even, even-odd or odd-even, and odd-odd nuclei, respectively, that are determined to reproduce fission cross sections of uranium isotopes [66]. In case of HFB-14, the information on barrier curvature, fission path, and the level density at the saddle points is provided [80,81], so we use them to calculate the fission transmission coefficients.

III. RESULTS

A. β-delayed neutron emission

In the last section, the width parameter Γ is introduced to make the β strength function a broad distribution. To determine the most likely Γ, we estimate the root mean squared (rms) value of P_{1n}, which is defined as

$$\sigma_{\rm rms}^{xn} = \sqrt{\frac{1}{N_{\rm expt}} \sum_{i}^{N_{\rm expt}} \left[\log_{10}\left(\frac{P_{xn,i}(c)}{P_{xn,i}(e)}\right)\right]^2}, \qquad (15)$$

where $N_{\rm expt}$ is the number of experimental data and $P_{xn}^{(i)}(c)$ and $P_{xn}^{(i)}(e)$ are the β-delayed neutron branching ratios of theoretical models and experiment of nucleus i, respectively. Note that in Ref. [26] a linear scaled rms is adopted to discuss the predictive power of P_{1n} calculated by the FRDM + QRPA + HFM [58]. However, we adopted logarithmic scaled rms as Eq. (15) because experimental P_{xn} extend from a small value of 10^{-2} to 10^2 as like half-lives.

Figure 2 shows $\sigma_{\rm rms}^{1n}$ as a function of width parameter Γ of the Gaussian type of Eq. (8) (dashed line) and the Lorentzian type of Eq. (9) (solid line). Experimental data are mainly taken from ENSDF [34], however, we replace the data if a new BDNE branching ratio reported in Ref. [82] is available. Below $\Gamma = 0.2$ (0.4) MeV for the Lorentzian (Gaussian) type, $\sigma_{\rm rms}^{1n}$ are more than 1.0, which means a factor of ten difference in P_{1n} on average. This is because β feedings above one neutron separation energy S_n are limited and P_{1n} is mostly underestimated. Increasing Γ, $\sigma_{\rm rms}^{1n}$ becomes smaller because some β strengths seep into energies above S_n and the majority of the calculated P_{1n} comes close to the experimental values. Although there exists a β strength function that escapes from the $1n$ emission energy window ($S_n \leqslant E^* < S_{2n}$) to x-neutron (xn) ones ($S_x \leqslant E^* < S_{(x+1)n}$), this outflow is generally smaller than the gain to the $1n$ emission energy window because β-decay rates become lower with increasing excitation energies. Eventually, $\sigma_{\rm rms}^{1n}$ takes a minimum value at $\Gamma = 0.6$ MeV for the Lorentzian type ($\sigma_{\rm rms}^{1n} = 0.602$) and at

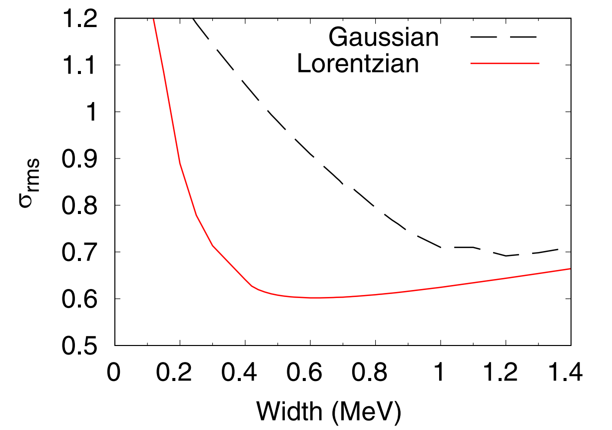

FIG. 2. Estimated $\sigma_{\rm rms}^{1n}$ value given in Eq. (15) as a function of the width Γ calculated with the Gaussian-type function (8) and the Lorentzian type function (9).

$\Gamma = 1.2$ MeV for the Gaussian type ($\sigma_{\rm rms}^{1n} = 0.694$). Above the minimal points, $\sigma_{\rm rms}^{1n}$ turn into a slow increase. This is because β strengths contribute too much at energies above S_n, and a majority of calculated P_{1n} becomes large as compared with experimental values.

The Lorentzian-type weight function gives a better result than the Gaussian one in terms of $\sigma_{\rm rms}^{1n}$. It is difficult to explain this because the result of $\sigma_{\rm rms}^{1n}$ is complicatedly convoluted by the many P_{1n} data. However, it is considered that the little leakage of the β strength function extending far outside of the mean of the Lorentzian function plays a significant role for the better agreement of P_{1n} with experimental data. In fact, the Gaussian-type weight function needs a wider width than the Lorentzian type to give the minimal $\sigma_{\rm rms}^{1n}$. In the subsequent sections in this paper, we discuss BDNE and BDF using the weight function of Lorentzian type with $\Gamma = 0.6$ MeV, the width of which is reasonable as compared with the experimental measurements of low-lying GT resonances for stable tin isotopes investigated by (^{3}He, t) reactions [83].

Table I lists $\sigma_{\rm rms}^{1n}$ of the pn-RQRPA + HFM together with the pn-RQRPA [15], Gross theory (GT2) [41,42], and FRDM + QRPA + HFM [58]. We also list $\sigma_{\rm rms}^{1n}$ classified by four different ranges of P_{1n}. The total value of $\sigma_{\rm rms}^{1n}$ was 0.798 for the pn-RQRPA. Note that, in the pn-RQRPA, the β strength functions are weighted by a Lorentzian function using a width of 130 keV that is determined so as to reproduce β-delayed neutron yield of thermal-neutron-induced fission of ^{235}U. The present result of pn-RQRPA + HFM greatly improves that of pn-RQRPA, providing $\sigma_{\rm rms}^{1n} = 0.601$, which is comparable to that of the GT2 ($\sigma_{\rm rms}^{1n} = 0.595$) and the FRDM + QRPA + HFM (0.512). Especially, we obtained a remarkable improvement in $\sigma_{\rm rms}^{1n}$ throughout from $1 \leqslant P_{1n} \leqslant 100$. Although $\sigma_{\rm rms}^{1n}$ is deteriorated in $P_{1n} < 1$, the result of pn-RQRPA + HFM is still slightly better than that of the FRDM + QRPA + HFM.

Figure 3(a) shows the ratio of P_{1n} for the pn-RQRPA + HFM to that for the pn-RQRPA as a function of mass number A. We can see that most of the data points are above unity, i.e., most of P_{1n} is increased by the present framework. The main reason for the increments is the use of the large Γ. Figures 3(b)

TABLE I. Result of $\sigma_{\rm rms}^{1n}$ defined by Eq. (15) for different ranges of $P_{1n}(e)$ (%).

Model	$P_{1n}(e) < 1$	$1 \leqslant P_{1n}(e) < 10$	$10 \leqslant P_{1n}(e) < 50$	$50 \leqslant P_{1n}(e) \leqslant 100$	All $P_{1n}(e)$ data
pn-RQRPA + HFM	0.952	0.446	0.570	0.317	0.601
pn-RQRPA	0.857	0.727	0.925	0.460	0.798
GT2	0.852	0.656	0.464	0.320	0.595
FRDM + QRPA + HFM	1.084	0.442	0.482	0.281	0.512
Number of nuclei	50	92	91	34	267

and 3(c) show the ratio of calculated P_{1n} to experimental P_{1n} (C/E) for the *pn*-RQRPA + HFM and the *pn*-RQRPA, respectively. The underestimations of P_{1n} (i.e., C/E < 1) for the *pn*-RQRPA are improved for the *pn*-RQRPA + HFM. We confirmed that 73% of P_{1n} corresponding to 193 nuclei are improved for the *pn*-RQRPA + HFM.

Figure 4 plots P_n in the $N-Z$ plane, which are calculated by the *pn*-RQRPA + HFM with HFB-14 fission-barrier data. The magic numbers ($Z, N = 20, 28, 50, 82, 126$) and possible magic number $N = 184$ are shown by the double lines. For nuclei close to the valley of stability, P_n are almost zero. As the neutron number increases, P_n are enhanced due to small S_{xn} and large Q_β of neutron-rich nuclei. We observe the odd-even dependence, especially for the Z direction in the bottom-right sector from $Z = 82$ and $N = 126$ and the upper-left sector from $Z = 82$ and $N = 184$. In general, looking at an isotonic chain, Q_β of odd-Z nuclei are larger than those of neighboring even-Z nuclei because of pairing correlations, while S_{xn} are less sensitive to Z numbers. As a consequence, we obtain the result that P_n of odd-Z nuclei are larger than neighboring even-Z nuclei, generating the odd-even dependence. As an example, the set of [Q_β(MeV), S_n(MeV)] for ^{220}Ir ($Z = 77$) is about [12.2, 2.3], while that for the neighboring nuclei ^{219}Os ($Z = 76$) and ^{221}Pt ($Z = 78$) are about [11.1, 1.7] and [9.9, 2.2], respectively. Around the mass regions $95 < Z < 101$ and $184 < N < 200$, P_n displays a patchy pattern. In this region BDF plays a role competing with BDNE. We discuss it later in Sec. III B.

One may notice that P_n abruptly decrease in a region from $Z \approx 65$, $N \approx 140$ to $Z \approx 80$, $N \approx 180$ forming a "valley" in Fig. 4. In this region the single-particle energy of neutron $1i_{11/2}$ state exceeds that of proton $1h_{11/2}$ states in terms of the canonical single-particle basis, allowing the 0^- FF transition with a low excitation energy. This is also seen in the ratio of the FF β decay rates to the total decay rates (Fig. 12 of Ref. [15]). Since the β decays via the 0^- transition mostly feed levels lower than neutron threshold energies, a sudden decrease of P_n occurs. However, with increasing neutron number, the energy difference of neutron $1i_{11/2}$ and proton $1h_{11/2}$ states extends, and 0^- FF transitions involving this configuration feed to excited states higher than S_{xn}. Eventually, P_n takes a high value again in the region close to the neutron drip line.

Figure 5 shows P_{xn} from $x = 1$ to 5 in the N-Z plane, which are calculated with the HFB-14 fission barrier data. Since $1n$ emission occurs most easily for neutron-rich nuclei at excited states, P_{1n} distribute in a wide range of the N-Z plane. However, in a region close to the neutron drip line, $1n$ emissions are no longer the major decay mode. Instead, multineutron emissions become significant due to large Q_β and low S_{xn}. Because the $2n$ emission channel is open at higher energy, P_{2n} extend in a more neutron-rich side than P_{1n}. Similarly, the distributions of P_{xn} gradually shift to the neutron drip line with increasing x.

We observe that P_{xn} in Fig. 5 do not spread over a simple straight band from low to heavy nuclei in the N-Z plane,

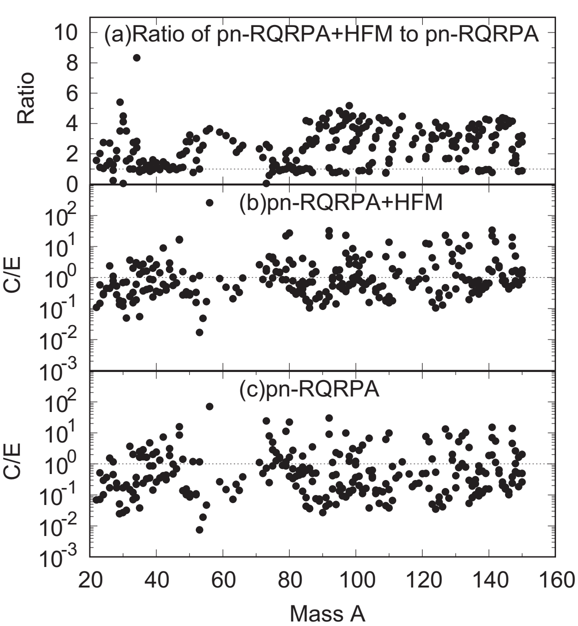

FIG. 3. (a) Ratio of P_{1n} for *pn*-RQRPA + HFM to that for *pn*-RQRPA. Panels (b) and (c) represent ratio of calculated to experimental data of P_{1n} (C/E) for *pn*-RQRPA + HFM (this work) and *pn*-RQRPA [15], respectively.

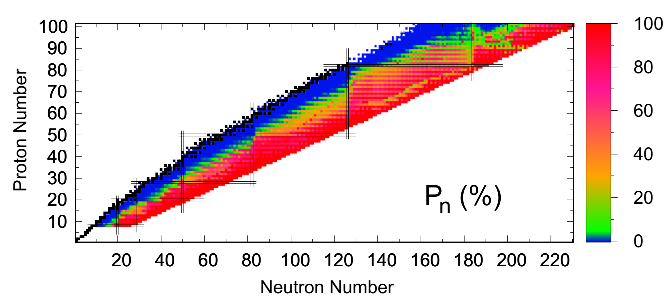

FIG. 4. Total β-delayed neutron branching ratios ($P_n = \sum_x P_{xn}$) calculated by the *pn*-RQRPA + HFM with HFB-14 fission barrier data [76]. The black filled squares stand for stable or long-lived nuclei.

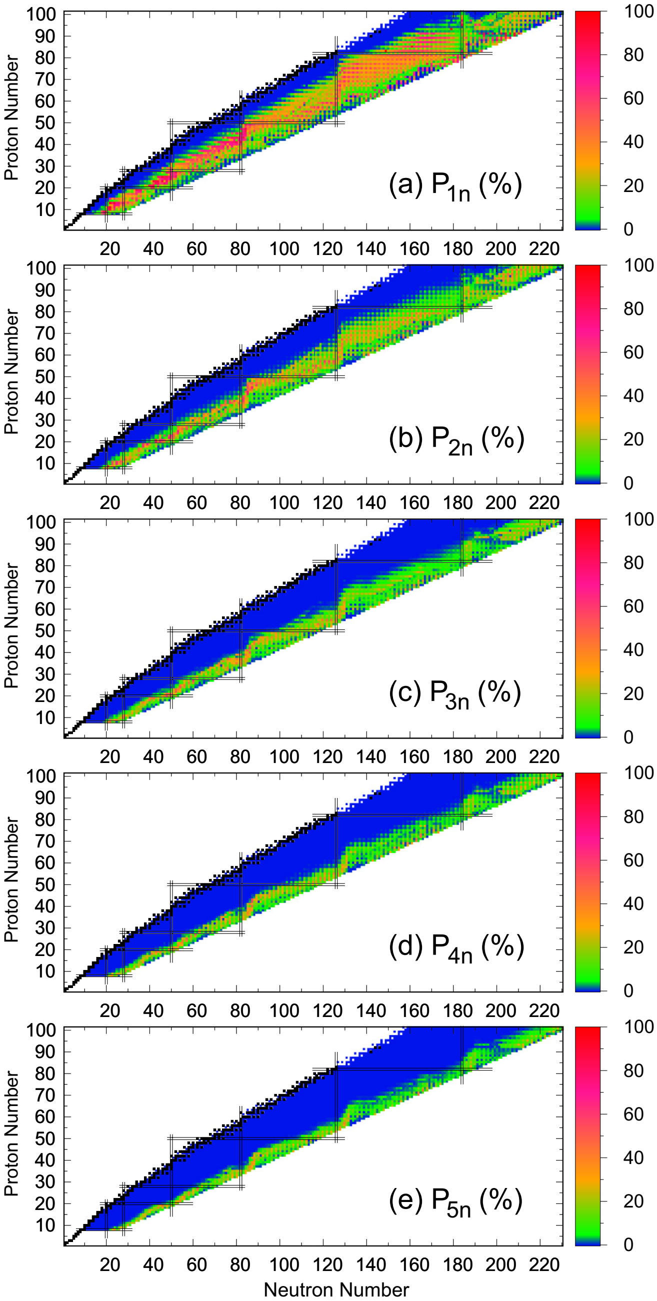

FIG. 5. β-delayed neutron branching ratio of P_{1n} to P_{5n} in the N-Z plane.

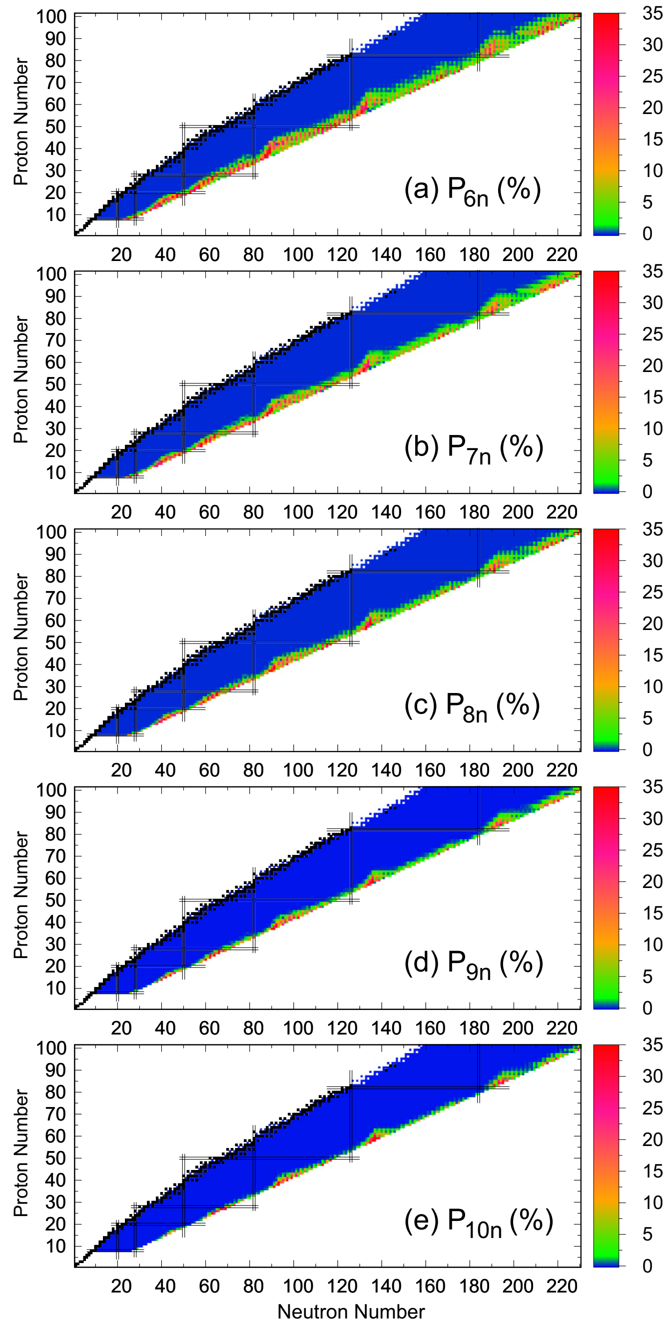

FIG. 6. Same as Fig. 5, but for P_{6n} to P_{10n}.

but show bends around neutron magic numbers $N = 50$, 82, 126, and 184. In general, nuclei with the magic numbers are strongly bound as compared with neighboring nuclei, while nuclei with a few more neutrons than the magic numbers are relatively weakly bound. As a result, S_{xn} of nuclei with a few more neutrons than the magic numbers are low and it is easy for those nuclei to emit neutrons from the highly excited states. Thus, P_{xn} tend to have a high value along the neutron magic numbers, making the bends.

In the work of pn-RQRPA [15], only up to $5n$ emissions are considered. However, through this study, we confirmed that $x > 5$ should have been considered for nuclei close to the neutron drip line. Figure 6 shows the $P_{xn}(6 \leqslant x \leqslant 10)$. Note that a different color scale from Fig. 5 is used to display the results clearly. With increasing x, the distribution of P_{xn} approaches the more-neutron-rich side, and the number of nuclei with a prominent P_{xn} significantly decreases. In the case of HFB-14 fission-barrier data, the number of nuclei with $P_{xn} > 10\%$ is 356, 254, 197, 121, and 91 for $x = 6$, 7, 8, 9, and 10, respectively. For P_{10n} only a limited nuclei near the neutron drip line show a meaningful value, especially around $Z = 26$ and $N = 65$, $Z = 40$ and $N = 95$, $Z = 55$ and

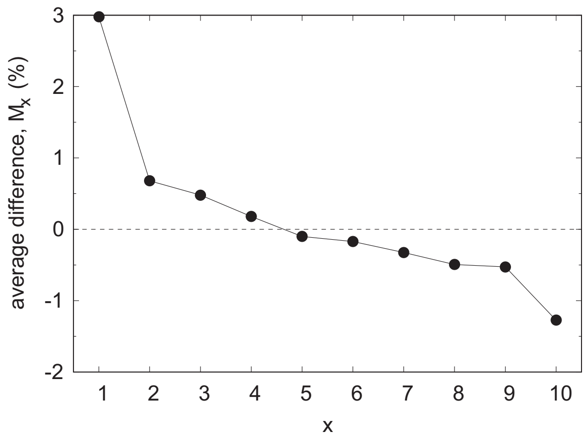

FIG. 7. Average difference M_x for various x defined in Eq. (16).

$N = 135$, and $Z = 85$ and $N = 195$, where the calculated Q_β value reaches about 20 MeV.

To see the variations from the *pn*-RQRPA that uses the cutoff method, we compute the average difference defined as

$$M_x = \frac{1}{N_N}\sum_i^{N_N}\left(P_{xn}^{(\mathrm{HFM})} - P_{xn}^{(\mathrm{cut})}\right). \tag{16}$$

where N_N is the number of nuclei and $P_{xn}^{(\mathrm{HFM})}$ and $P_{xn}^{(\mathrm{cut})}$ are β-delayed branching ratios of the *pn*-RQRPA + HFM and the *pn*-RQRPA. The result is shown in Fig. 7. Upon increasing x, M_x decreases monotonically and become negative for $x \geqslant 5$. This indicates that the BDNE branching ratios for low neutron multiplicity are increased in the present approach, while they are decreased for high neutron multiplicity.

To understand the difference of the results between the *pn*-RQRPA + HFM and *pn*-RQRPA further, we plot the β strength function of GT transition and xn emission energy windows in Fig. 8(a) in case of ^{140}Sn as an example. We can see that the most of the β strengths locate in the $1n$ emission energy window. Since the amount of the β-strengths to xn emission energy window directly becomes P_{xn} in the cutoff method, P_{1n} will be large for the *pn*-RQRPA.

On the other hand, in the *pn*-RQRPA + HFM, the BDNE branching ratios are calculated through multiplying the β strength functions by the isotope production ratios p_i, as in Eq. (10). Namely, the isotope production ratio mainly governs the difference of P_{xn} between the *pn*-RQRPA + HFM and the *pn*-RQRPA. Figure 8(b) shows p_i of Sb isotopes as a function of the excitation energy of the daughter nucleus ^{140}Sb. Until $S_n = 2.3$ MeV, p_i of ^{140}Sb is unity. Namely, only γ deexcitation occurs for ^{140}Sb without emitting any neutron. Entering the $1n$ emission energy window from $E^* = S_n$, p_i of ^{139}Sb suddenly becomes almost one and that of ^{140}Sb becomes almost zero. If the n-γ competition plays a role for this nucleus, the curves of p_i of ^{139,140}Sb at $E^* = S_n$ become more smooth [55]. Upon further increasing the energy, p_i of ^{139}Sb begins to decrease from $S_{2n} = 5.9$ MeV and that of ^{138}Sb becomes dominant from $E^* \approx 7$ MeV. A remarked point is that p_i of ^{138}Sb extend into not only the $2n$ emission energy window but the $3n$ emission energy window. This wide distribution is due to a

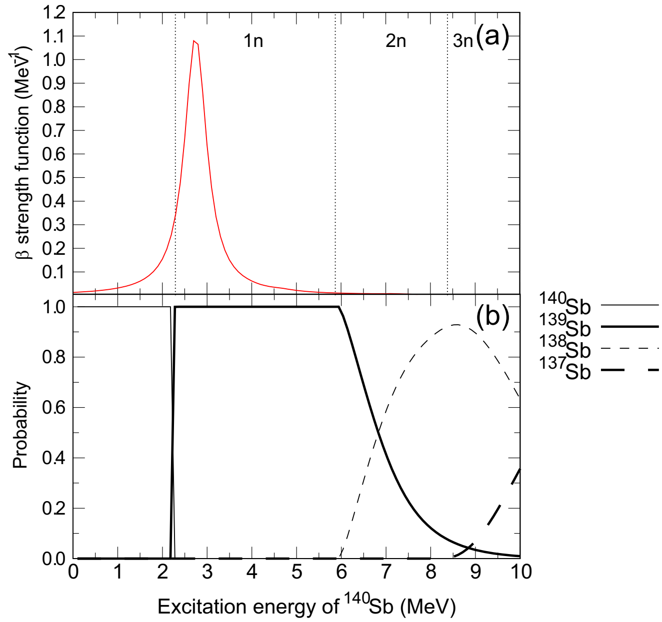

FIG. 8. (a) β strength function of ^{140}Sn. x-neutron (xn) emission energy windows are separated by the dotted lines. (b) Isotope production ratios, p_i of $^{137-140}$Sb as a function of excitation energy, assuming 1^+ excited states of ^{140}Sb (the daughter nucleus of ^{140}Sn). The calculation is performed by the HFM.

competition with $1n$ and $3n$ neutron-emission channels. However, the results of the *pn*-RQRPA and *pn*-RQRPA + HFM will be almost the same because there are no significant β strengths above the $2n$ emission energy window. Table II lists P_{xn} of ^{140}Sn for the *pn*-RQRPA + HFM and the *pn*-RQRPA [15], in which the contributions from the FF transitions are included in addition to the GT transition. We can see that the results of the *pn*-RQRPA + HFM and the *pn*-RQRPA show a good agreement in this nucleus. Namely, the cutoff method works well only if $0n$ and $1n$ emissions are the major decay channel, like this case. We should mention that P_{0n} and P_{1n}

TABLE II. β-delayed neutron branching ratios (in units of %) of ^{140}Sn and ^{162}Sn calculated by the *pn*-RQRPA + HFM and the *pn*-RQRPA.

	^{140}Sn		^{162}Sn	
Model	*pn*-RQRPA + HFM	*pn*-RQRPA	*pn*-RQRPA + HFM	*pn*-RQRPA
P_{0n}	62.6	57.7	12.5	10.4
P_{1n}	36.8	41.7	34.2	19.1
P_{2n}	0.6	0.3	12.9	15.7
P_{3n}	0.1	0.1	17.7	20.2
P_{4n}	0.0	0.0	7.1	1.5
P_{5n}	0.0	0.0	13.6	9.4
P_{6n}	0.0	0.0	1.2	1.4
P_{7n}	0.0	0.0	0.7	20.1
P_{8n}	0.0	0.0	0.1	0.6
P_{9n}	0.0	0.0	0.0	0.8
P_{10n}	0.0	0.0	0.0	0.8

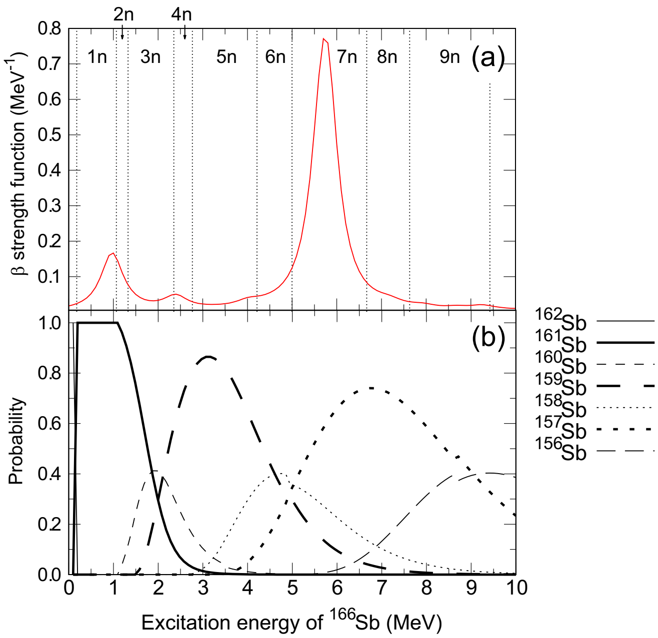

FIG. 9. (a) β strength function of ^{162}Sn. xn emission energy windows are separated by the dotted lines. (b) Isotope production ratios of $^{162\text{–}156}$Sb from 1^+ excited states of ^{162}Sb (the daughter nucleus of ^{162}Sn) as a function of excitation energy. The calculation is performed by the HFM.

are also largely different from those estimated by the cutoff method if the n-γ competition would be significant [55].

As going to more neutron-rich nuclei, the difference between the pn-RQRPA and the pn-RQRPA + HFM becomes striking. Figure 9 shows the β strength function of ^{162}Sn and the isotope production ratios of Sb isotopes in the case of the GT transition. The $1n$-to-$9n$ emission energy windows exist closely up to $E^* = 10$ MeV and the $2n$ emission energy window is at much lower energy than ^{140}Sn. The most significant β strengths are in the $7n$ emission energy window, so that P_{7n} is expected to be large in the cutoff method. On the other hand, looking at Fig. 9(b), p_i of different isotopes distribute into a wide range of excitation energy and are not stuffed inside a specific neutron-emission energy window. As mentioned, this wide distribution ranging over various neutron-emission energy windows is due to the competition with $1n$, $2n$, and multineutron-emission channels. In the $7n$ emission energy window, p_i of $^{156\text{–}159}$Sb isotopes exist side by side. Note that p_i of ^{155}Sb produced by $7n$ emission is about zero in the $7n$ emission energy window, so that P_{7n} will be almost zero in the pn-RQRPA + HFM. This mismatch comes about because the daughter nucleus and descendant nuclei lost their excitation energy every time neutrons are emitted. This never happens in the framework of the cutoff method. The results of P_{xn} for the pn-RQRPA + HFM and the pn-RQRPA are listed in Table II, in which they show a large difference. We notice that $P_{7n} = 20\%$ for the pn-RQRPA, but 0.7% for the pn-RQRPA + HFM. The missing fraction of P_{7n} is redistributed to P_{xn} with $x \leqslant 6$. Note again that contributions from the FF transitions are included in the result of Table II.

In the cutoff method, P_{xn} with a large x can have a finite value if it is energetically allowed. However, excitation energy of nuclei is wasted every time neutrons are emitted. As a consequence, the relative difference of P_{xn} between the cutoff method and the HFM becomes larger as nuclei have lower S_{xn} and higher Q_β that enable multineutron emission. As seen in Fig. 7, P_{xn} for $x \geqslant 5$ become negative due to this reason. The reduced fractions in $x \geqslant 5$ turn into P_{xn} for $x \leqslant 4$. Since P_{10n} do not obtain a backward flow from higher x, the reduction is larger than others.

Figure 10 shows P_{1n} of Pd ($Z = 46$) and Ag ($Z = 47$) isotopes that are considered as important β-delayed neutron precursors in the r process [16], and Os ($Z = 76$) and Ir ($Z = 77$) isotopes. We plot the results of the FRDM + QRPA + HFM [58] for comparison. The result of pn-RQRPA + HFM shows a P_{1n} similar to that of the FRDM + QRPA + HFM for nuclei with small mass numbers. Upon going toward heavier mass, the two calculations begin to differ. The noticeable contrasts are found in nuclei close to the neutron drip line and $210 \leqslant A \leqslant 230$ for Os and Ir isotopes. A major factor affecting P_{1n} is the β strength function and one neutron separation energies S_n that are calculated from the theoretically predicted mass data, for which the pn-RQRPA + HFM and the FRDM + QRPA + HFM use the global nuclear mass model [74] and FRDM2012 [84], respectively. For most of nuclei close to the drip line, S_n of the global nuclear mass model is lower than those of FRDM; for example, S_n of ^{240}Ir is 269 keV for the global mass model and 690 keV for FRDM2012. To check the sensitivity of P_{1n} to mass data, we carry out the same calculation replacing the mass data of the pn-RQRPA + HFM with FRDM2012 and find that the result for nuclei near the drip line globally becomes close to that of the FRDM + QRPA + HFM. However, P_{1n} in $210 \leqslant A \leqslant 230$ for Os and Ir isotopes still differ significantly. We thus consider that the deviations found in $210 \leqslant A \leqslant 230$ for Os and Ir isotopes are mainly attributed to the β strength function and those found near the neutron drip line is due to the mass data.

In this work, if daughter nuclei in the ground state are unstable against neutron emissions, i.e., for the case of $S_n = 0$ MeV, we let them emit one neutron automatically. Therefore, P_{0n} of corresponding nuclei become zero and the fraction shifts to P_{1n}. One can see the effect in Fig. 10, which shows odd-even staggering for nuclei near the neutron drip line. For example, P_{1n} for ^{150}Pd is about 40%, while that for ^{149,151}Pd is almost zero. The remarkably high fraction of P_{1n} for ^{150}Pd is because the daughter nucleus ^{150}Ag is a neutron-unbound nucleus according to the global nuclear mass model [74]. On the other hand, ^{149,151}Ag is stable against neutron emission, keeping P_{1n} small.

We also computed delayed-neutron yield of thermal-neutron-induced fission of ^{235}U. The result is shown in Table III. The fission-fragment yields of thermal-neutron-induced fission of ^{235}U are taken from JENDL Fission Product Yield 2011 (JENDL/FPY2011) [85,86]. The pn-RQRPA gives the β-delayed neutron yield closest to the experimental data among the four models because the P_n are tuned to reproduce it. The result of pn-RQRPA + HFM also reproduces the experimental data in the same order. Note that the calculated delayed neutron yields are an aggregated value

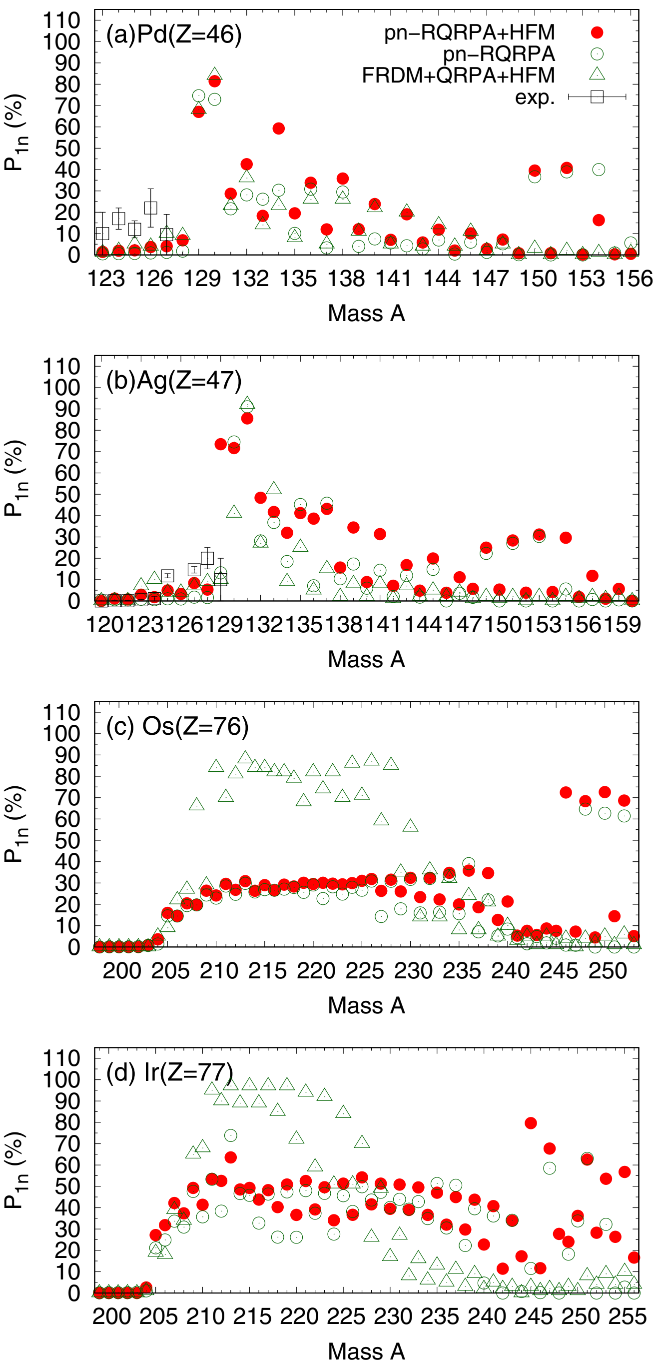

FIG. 10. β-delayed neutron branching ratio P_{1n} of Pd, Ag, Os, and Ir isotopes as a function of A. The experimental data are taken from Ref. [82].

summed over fission-fragment yields. Looking into important precursor nuclei contributing the delayed neutron yield, the result of *pn*-RQRPA is not necessarily correct. For example, a precursor contributing the delayed neutron yield the most is ^{137}I [$P_{1n}(e) = 7.66\%$ [34]] according to the recent evaluation [82], while it is ^{91}Rb for the *pn*-RQRPA calculation and ^{137}I enters the eighth place with $P_{1n} = 0.7\%$. On the other hand, the *pn*-RQRPA + HFM calculation shows ^{137}I to be the most important precursor, however, the P_n ($\approx$2.25%) is still

TABLE III. β-delayed neutron yield of thermal-neutron-induced fission of ^{235}U. Fission-fragment yields are taken from JENDL/FPY-2011 [85,86].

Model	β-delayed neutron yield
pn-RQRPA	1.43×10^{-2}
pn-RQRPA + HFM	1.00×10^{-2}
GT2	0.81×10^{-2}
FRDM + QRPA + HFM	0.81×10^{-2}
Expt. [87]	$(1.58 \pm 0.05) \times 10^{-2}$

underestimated and thus the calculated delayed neutron yield is smaller than the experimental value.

The advantage of using the HFM is that one can estimate the spectra of emitted particles. In particular, a high interest is paid to delayed neutron spectra, which are expected to be used for nondestructive analysis of nuclear materials [88,89]. However, it is difficult to measure delayed neutron spectra systematically for nuclei in the nuclear chart. Therefore, theoretical predictions are used to fill out the lack of the evaluated nuclear data such as ENDF/B-VIII.0 [90] and forthcoming JENDL-5 if no experimental data are available. As an example, Fig. 11

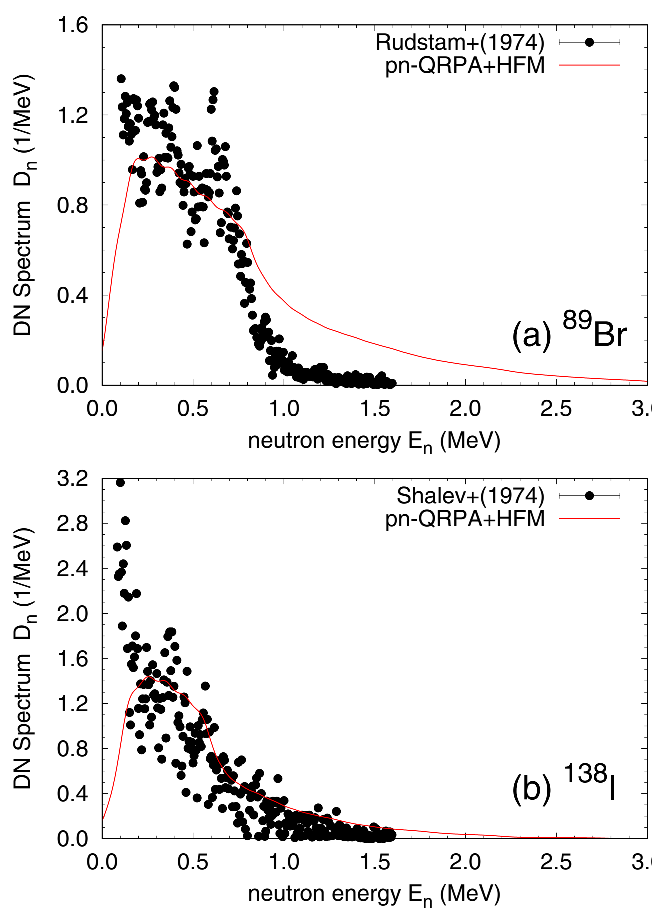

FIG. 11. BDNE spectrum of (a) ^{89}Br and (b) ^{138}I. The calculated result is shown by the solid line (red). Experimental data are taken from Rudstam *et al.* [91] and Shalev *et al.* [92].

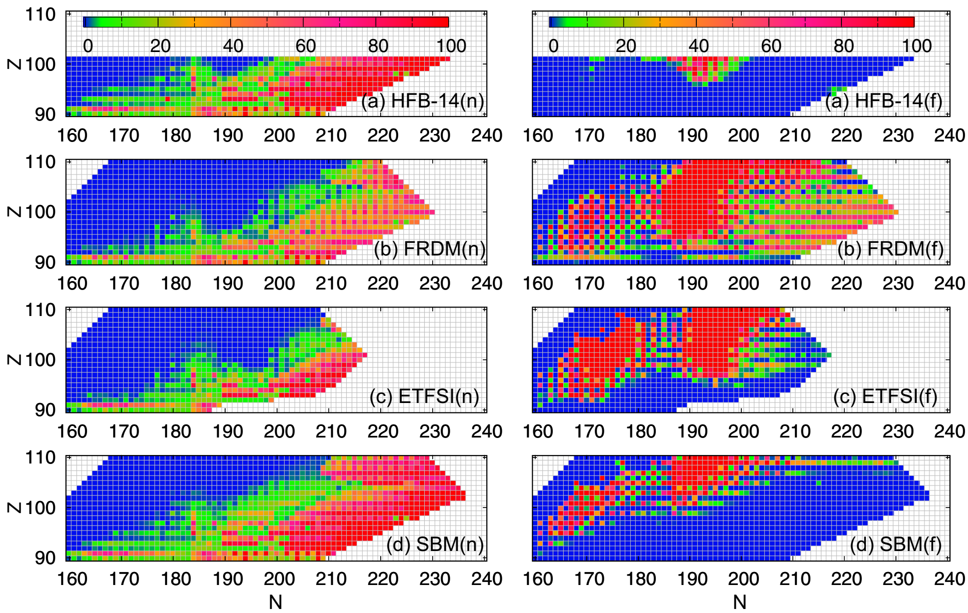

FIG. 12. BDNE branching ratios P_n (left panels) and BDF branching ratios P_f (right panels) in unit of % calculated by the fission barrier data of (a) HFB-14 [76], (b) FRDM [78], (c) ETFSI [77], and (d) SBM [79]. Nuclei where no fission barrier or β-decay data are provided are given as blank.

shows the BDNE spectrum of ^{89}Br and ^{138}I, which are typical β-delayed neutron precursors. We also plot the experimental data taken from Refs. [91,92]. Although fine structures observed in the experimental data are not reproduced well by the pn-RQRPA + HFM, the computed results reasonably emulate the experimental β-delayed neutron spectra.

B. Effect of β-delayed fission

Figures 12(a)–(d) show BDNE and BDF branching ratios for $Z \geqslant 90$ in the N-Z plane using different fission barrier data of HFB-14 [76], FRDM [78], ETFSI [77], and SBM, respectively [79]. Note that nuclei where no fission barrier or β-decay data are provided are given as blank. As is obvious, for nuclei where P_f is significant, P_n is small since they are correlated. We can see that P_n and P_f greatly vary among the fission barrier data. A common feature is that BDF branching ratios become high around $93 \leqslant Z \leqslant 110$ and $184 \leqslant N \leqslant 200$ for FRDM, ETFSI, and SBM. Although the number of nuclei calculated in this region is limited for HFB-14, P_f become meaningful as well around $Z = 100$ and $N = 190$. BDF is also significant from $Z = 91$, $N = 160$ to $Z = 100$, $N = 185$ for FRDM, ETFSI, and SBM, while that for HFB-14 is negligibly small. There exists an odd-even dependence for P_f in the region of $N = 160$ to 185, in particular, for FRDM and SBM. This odd-even dependence is also found in Ref. [26], which calculates P_f with the FRDM + QRPA and the FRDM barrier data [78]. An effect of the neutron magic number of $N \approx 184$ is seen for ETFSI and weakly for FRDM and SBM. On the neutron-rich side, P_n become major for HFB-14, ETFSI, and SBM, while BDNE and BDF compete with each other for FRDM.

Figure 13 shows P_{1n} and P_{1nf} calculated with the different fission barrier data for $Z \geqslant 90$ in the N-Z plane. The number of nuclei showing a significant P_{1nf} is much less than P_f. This means that most nuclei do fission directly after β decay without emitting neutrons in a high probability. However, FRDM still has relatively many nuclei with prominent P_{1nf} as compared with the other fission barrier data. As will be discussed later, this is because fission barrier of FRDM is low and single-humped. Figure 14 shows the result of P_{2n} and P_{2nf}. The number of nuclei having a significant P_{2nf} is even less than that of P_{1nf}. In particular, there are few nuclei showing a prominent P_{2nf} for HFB-14 and SBM, and accordingly their distributions of P_{2n} become similar to each other. On the other hand, there are still a lot of nuclei with prominent P_{2nf} in the neutron-rich region for FRDM. ETFSI also shows some nuclei that have compelling P_{2nf}.

Figure 15 shows the result for P_{3nf}. For HFB-14 and SBM, only a few nuclei show a prominent P_{3nf}. Thus the distribution of P_{3n} is almost the same. In our calculation, P_{3nf} of all nuclei are less than 10% for HFB-14, ETFSI, and SBM, while there are still a number of prominent P_{3nf} in neutron-rich sides for FRDM. We also plot P_{4n} and P_{4nf} in Fig. 16. There are a couple of nuclei that give a significant P_{4nf} for ETFSI and no compelling P_{4nf} for HFB-14 and SBM. Even for FRDM, only limited nuclei show a prominent P_{4nf}. In Fig. 17, no significant P_{5nf} is observed for HFB-14, ETFSI, and SBM, and the results of P_{5n} are almost the same at least for the nuclei where the calculation is done. For FRDM, there are still nuclei that have a prominent P_{5nf}, however, the number is decreased from P_{4nf}. We confirm that $P_{xnf} (x \geqslant 6)$ are less than 1% for HFB-14, ETFSI, and SBM, while those for FRDM are still large, especially for nuclei with odd Z from 93 to 103. An importance of multichance fission has been pointed out using the FRDM fission barrier data [26]. However, it is seen from this work that the importance of multichance fission strongly depends on fission barrier data.

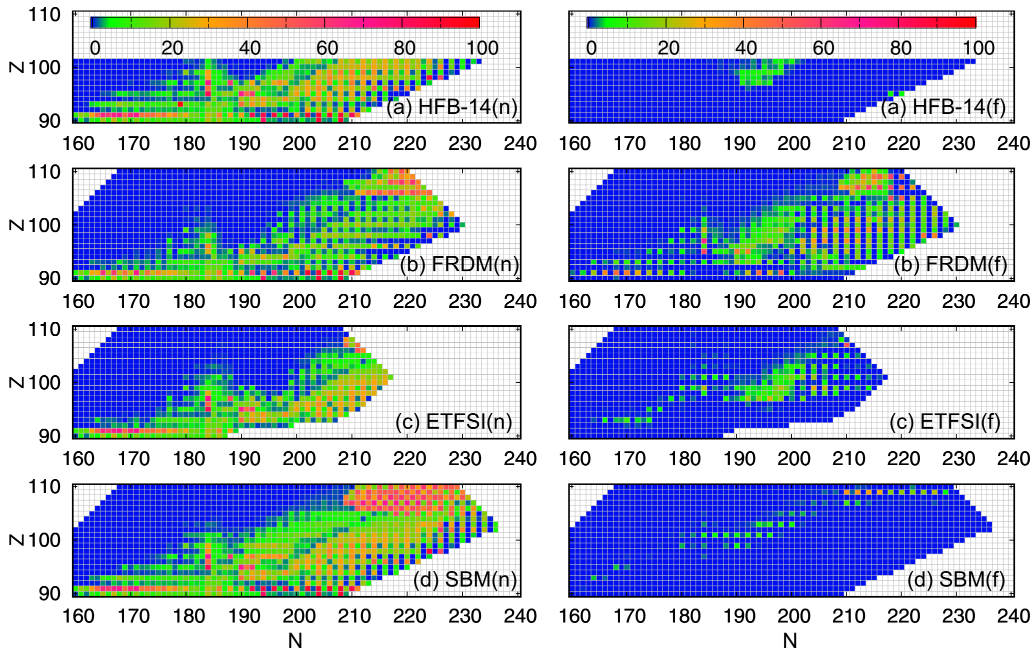

FIG. 13. Same as Fig. 12, but for P_{1nf}.

To understand the result of P_{xnf} more qualitatively, we plot fission barrier heights (B_f) of fermium isotopes used in this work in Fig. 18. The numbers in parentheses for the HFB-14 indicate the (1) inner, (2) middle, and (3) outer fission barriers. Similarly, the numbers in parentheses for the ETFSI indicate (1) inner and (2) outer fission barriers. The fission barrier of SBM is as high as the other fission barrier data for $160 \leqslant N \leqslant 185$, while it becomes significantly larger above $N = 186$. Thus, P_f of SBM are comparable to the other fission barrier data around $Z = 100$, $N = 170$, while they are strongly hindered for the neutron-rich region. HFB-14 has triple fission barriers. Although the inner barrier height decreases from $N = 160$ to 178, the middle and outer barriers emerge from $N = 170$. This triple-humped structure strongly hinders the fission rates and P_f in this region, as we have seen in Fig. 12. Around $N = 190$, the inner and middle barrier heights are low and the outer barrier is irrelevant so that P_f become significant in this region. With increasing neutron number, the inner and

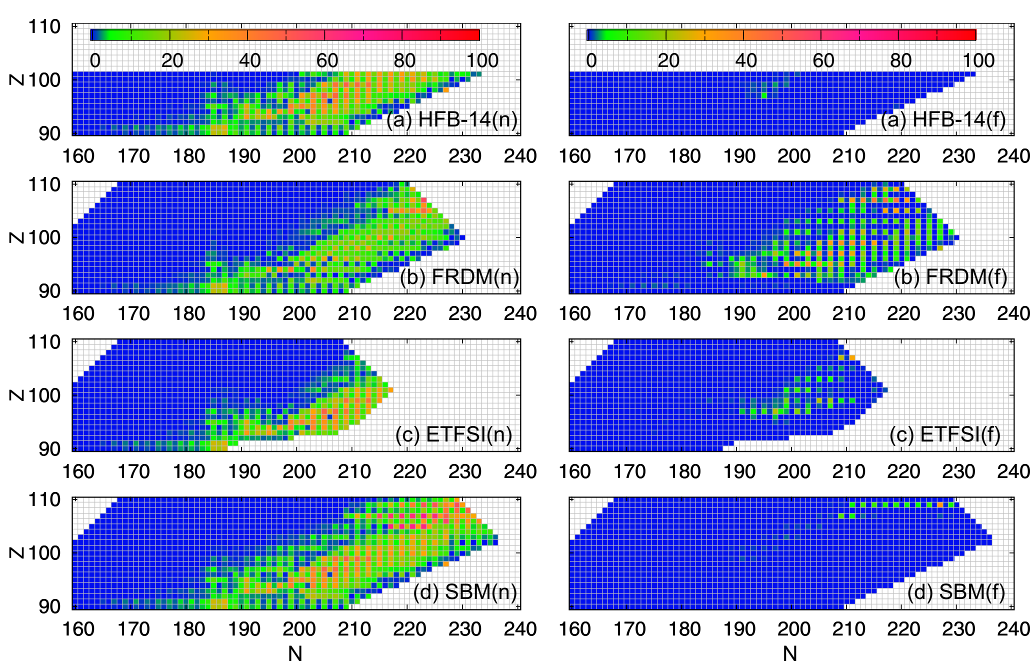

FIG. 14. Same as Fig. 12, but for P_{2nf}.

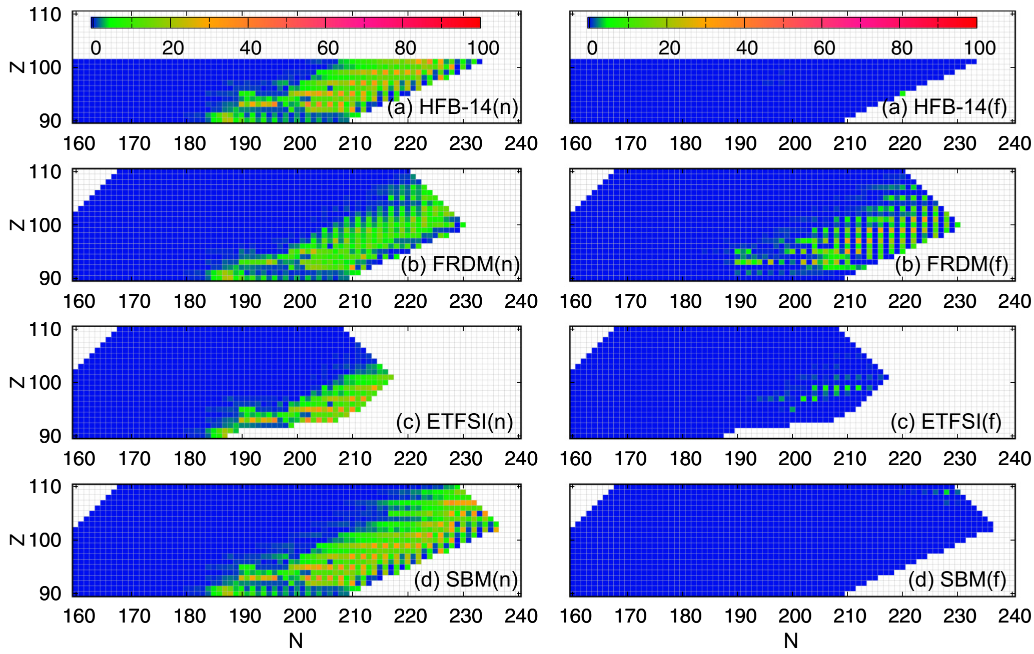

FIG. 15. Same as Fig. 12, but for P_{3nf}.

middle barriers become high again and the fission rates are again hindered. Similar to HFB-14, the inner barrier of ETFSI decreases from $N = 160$ to 172. However, the barrier heights are about 2 MeV lower than HFB-14 and BDF competes with BDNE. As a result, P_f for ETFSI are significant in this region, in contrast with HFB-14. From $N = 173$, the inner barrier increases and peaks around $N = 183$. This fact makes P_f of ETFSI less important, showing the valley in this region as seen in Fig. 12. The outer barrier which emerges from $N = 183$ would also have a meaningful effect on forming the valley. Above $N = 192$, the inner barrier of the ETFSI shows a behavior similar to that of HFB-14. However, P_f of ETFSI is larger than that of HFB-14 because ETFSI is a single-humped barrier while HFB-14 gives a double- or triple-humped fission barrier in this region. The barrier heights of FRDM are rather constant ($B_f \approx 4$ MeV) except in $184 \leqslant N \leqslant 200$, where B_f are close to the inner and middle barriers of HFB-14. In spite of that, the reason why the FRDM has more prominent P_{xnf}

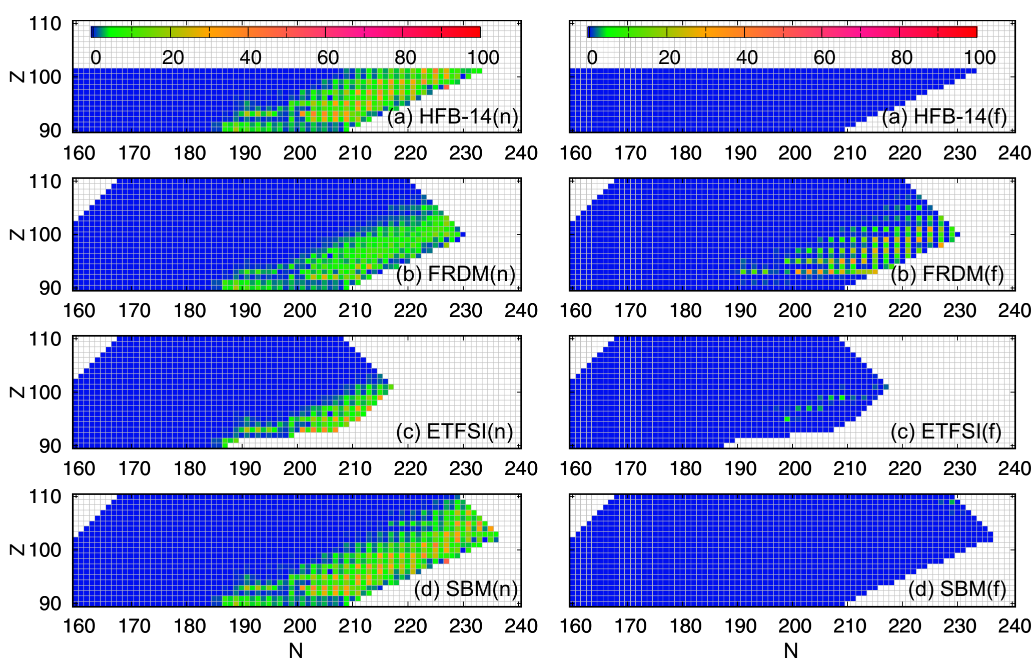

FIG. 16. Same as Fig. 12, but for P_{4nf}.

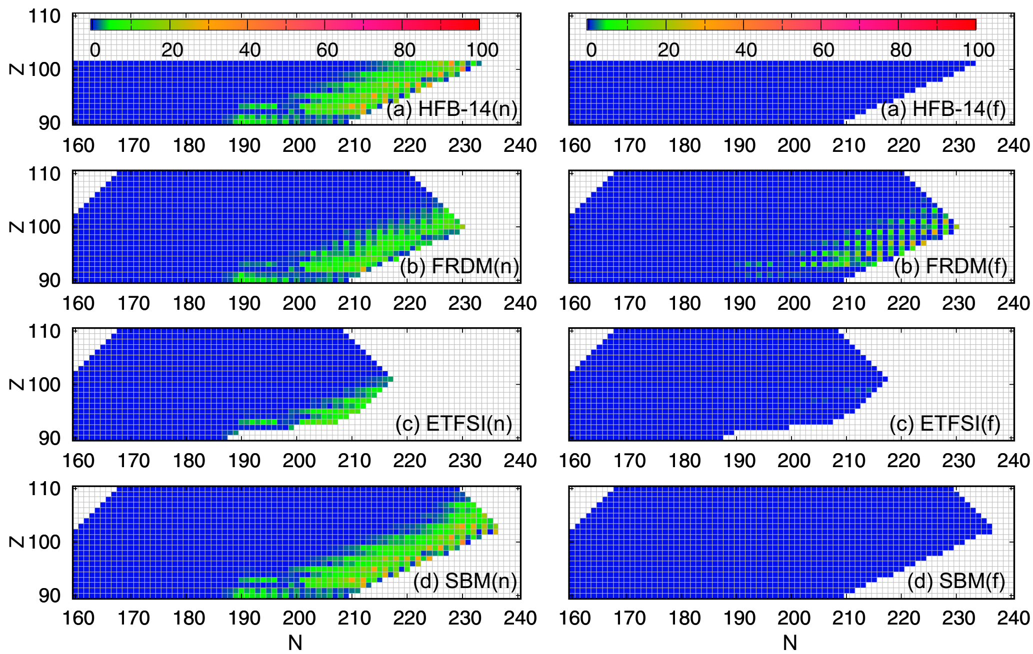

FIG. 17. Same as Fig. 12, but for P_{5nf}.

in this region is that HFB-14 as well as ETFSI have a double- or triple-humped barrier. The importance of BDF is thus not determined only by the fission barrier height but by the number of barrier humps. The SBM also provides a single barrier, however, the barrier height is larger than for the FRDM and P_f are significantly reduced.

C. β-delayed α emission

In this work, we allow daughter nuclei also to decay by α-particle emission and study the β-delayed α emission branching ratio P_α as well as BDNE and BDF. The calculated P_α are shown in Fig. 19. Note that the maximum scale is set to be $P_\alpha = 10\%$ for illustration. Because we found that nuclei where β-delayed α emission is prominent are not affected by the selection of fission barrier data, the results in the case of the FRDM fission barrier data are plotted. Since neutron emission overcomes α-particle emission in the neutron-rich region, a non-negligible P_α is observed only in a band of near the valley of stability. To our knowledge, experimental data on β-delayed α-particle emission has been reported only for ^{214}Bi ($P_\alpha = 0.003\%$) [81,93] in the range of Fig. 19. The calculated result of P_α for ^{214}Bi is 0.026%. Although our model overestimates the experimental data, it shows that the β-delayed α-particle emission branching ratio is very small.

Exceptional cases exceeding $P_\alpha = 10\%$ are ^{210,211}Bi ($Z = 83$) and ^{248}Am ($Z = 95$), that have $P_\alpha = 92.5\%$, 48.9%, and 15.9%, respectively. The daughter nuclei ^{210,211}Po and ^{248}Cm have a relatively high α-decay rates from the ground states [93]. It is not thus surprising that they do α-particle emission following β decay, competing with γ and other deexcitations. We checked delayed proton emission branching

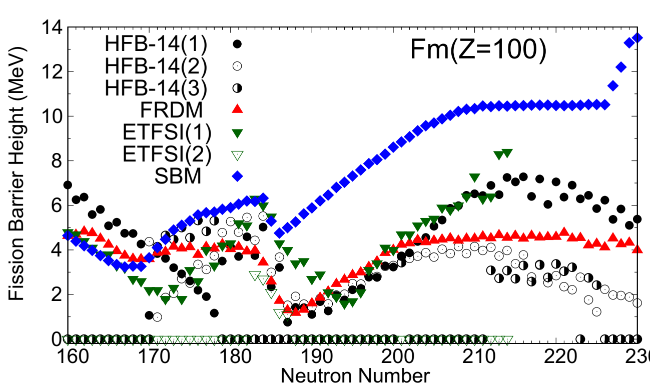

FIG. 18. Fission barrier height of Fm ($Z = 100$) isotopes for HFB-14 [76], FRDM [78], ETFSI [77], and SBM [79] models. The numbers in parentheses indicate 1 : inner, 2 : middle, and 3 : outer fission barrier heights.

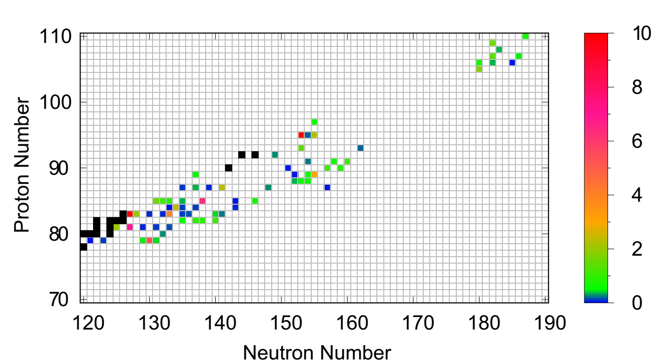

FIG. 19. Delayed alpha branching ratios P_α (%) in the case of FRDM fission barrier data. The black filled squares indicate stable or long-lived nuclei.

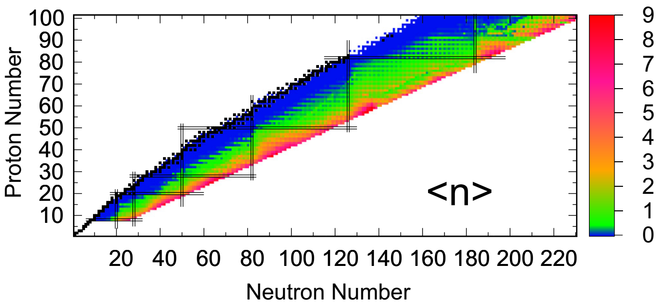

FIG. 20. Mean number of emitted neutrons in the N-Z plane. The calculation is performed by the HFB-14 fission barrier data [76].

ratios P_p as well; however, no significant P_p is obtained in this work. Note that our calculation is carried out only for nuclei in the β-stability line to a neutron-rich region. Our future plan is to study a neutron-deficient region where it is expected that P_α as well as P_p become more important than P_n.

D. Number and energy of emitted neutrons

From the β-delayed neutron branching ratios and spectra, we can also calculate the mean number and the mean kinetic energy of emitted neutrons that are defined as

$$\langle n\rangle = \sum_x x(P_{xn} + P_{xnf} + P_{xn\alpha} + P_{xnp}) \tag{17}$$

and

$$\langle E_n\rangle = \int E_n D_n(E_n) dE_n, \tag{18}$$

respectively. Those quantities are important for examining the r-process final abundance after the freeze-out phase. Note that neutrons can be also provided from highly excited fission fragments, known as prompt neutrons. However, the results discussed in this work are limited to β-delayed neutrons since the prompt neutrons are beyond our scope.

Figure 20 shows the mean number $\langle n\rangle$ of β-delayed neutrons in the N-Z plane. As expected, the value of $\langle n\rangle$ near the valley of the stability is small, while it becomes prominent as the neutron number increases. In our calculation, the maximum $\langle n\rangle$ is about 9.7 for ^{192}La, which is in the spot showing a prominent P_{xn} even for a large x, as we have seen in Fig. 6. We also plot the mean neutron numbers for nickel, tin, and fermium isotopes for the pn-RQRPA + HFM and the pn-RQRPA in Fig. 21. For most nuclei, the mean neutron number is less than 1. From the appreciably-neutron-rich side where the neutron number is approximately double the proton number, $\langle n\rangle$ begins to increase significantly, being more than 1. The difference between the pn-RQRPA + HFM and the pn-RQRPA is not large for nuclei with a relatively small A, while $\langle n\rangle$ of the pn-RQRPA + HFM becomes significantly smaller than those of pn-RQRPA as the neutron number increases, because excitation energies to be used for neutron emissions are reduced effectively by β-delayed neutrons, as discussed in the previous section. For nuclei at the neutron drip line, the deviations of $\langle n\rangle$ from the pn-RQRPA

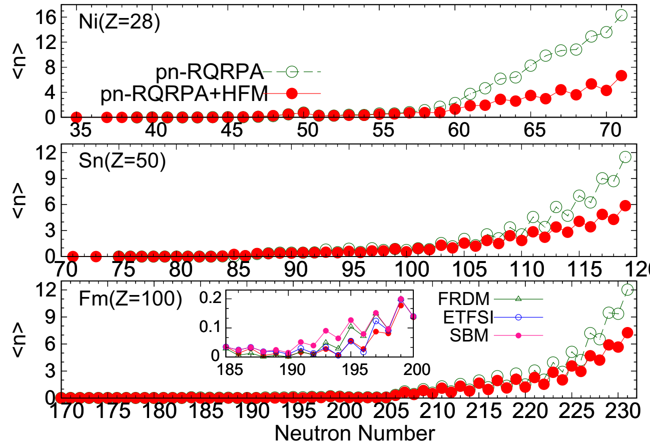

FIG. 21. Mean number of emitted neutrons for nickel, tin, and fermium isotopes.

that uses the cutoff method are approximately a factor of two.

We also plot the results with different fission barrier data for fermium isotopes ($185 \geqslant N \geqslant 200$) in the inset of Fig. 21. The mean neutron number of SBM is the largest in this mass region, although the variation of $\langle n\rangle$ among the fission barrier data is rather small. This is because the fission rates of SBM are low due to the high fission barriers as seen in Fig. 18, and the chances for emitting more neutrons are enhanced instead of fission. The difference among fission barrier data becomes negligible as going to the neutron drip line because P_f are commonly much smaller than P_n. Figure 22 shows the mean energy of β-delayed neutrons. In the region of light nuclei around $8 \leqslant Z \leqslant 28$, the mean energy is relatively large, while it becomes smaller as going to heavier nuclei. The average energy $\langle E_n\rangle$ for $Z \leqslant 28$ is 935 keV, while that for $Z > 28$ is 432 keV. In addition, $\langle E_n\rangle$ tend to be high for nuclei just above the neutron magic number, especially for $N = 28$, 50, and 82.

The kinetic-energy distribution of an emitted neutron, $X_n(\epsilon_n)$, is approximately expressed by

$$X_n(\epsilon_n) \propto \rho_N(E^* - \epsilon_n - S_n)\rho_n(\epsilon_n), \tag{19}$$

where $\rho_N(E)$ and $\rho_n(\epsilon_n)$ are the level density of decayed nuclei with an excitation energy of E and the phase space of the emitted neutron with the kinetic energy ϵ_n, respectively. In

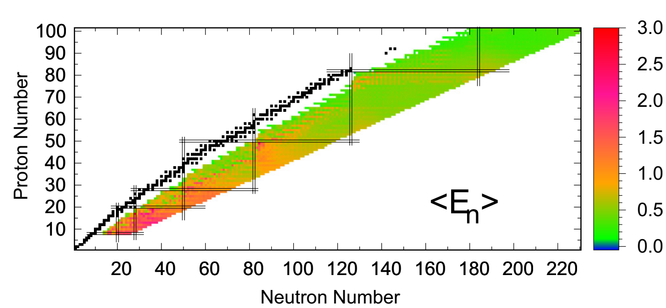

FIG. 22. Mean energy of emitted neutrons in the N-Z plane.

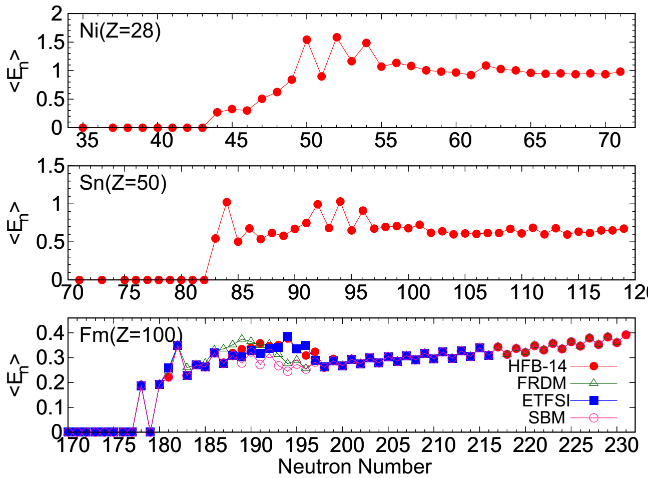

FIG. 23. Mean energy of β-delayed neutron $\langle E_n \rangle$. For fermium isotopes, the results with different fission barrier data are also plotted together.

general, the level density exponentially grows as the excitation energy increases. Thus a transition to higher levels is the most likely, however, the phase space of the outgoing neutron becomes small instead. For light nuclei and nuclei around the neutron magic numbers, the level densities are relatively low even at a high excitation energy and thus emitted neutrons can have a large phase space easily. On the other hand, the level densities of heavy nuclei rapidly increase as the excitation energy goes up, the phase space of neutron is limited, and the kinetic energy becomes low.

We plot the mean energy for nickel, tin, and fermium isotopes in Fig. 23. For comparison, we also plot the results with different fission barrier data in the case of fermium isotopes. For nickel isotopes, $\langle E_n \rangle$ gradually increase and become relatively high for $N = 50$, 52, and 54. The high mean energies are mainly due to the $N = 50$ magic number, as discussed above. Upon increasing the neutron number, $\langle E_n \rangle$ almost become constant around 1 MeV. For tin isotopes, we can see again that the mean energy is locally high for $N = 84$ just above the neutron magic number $N = 82$. The mean energy becomes $\langle E_n \rangle \approx 0.6$ MeV upon increasing the neutron number. For fermium isotopes, $\langle E_n \rangle$ are about 0.3 to 0.4 MeV, which are only about one-third of nickel isotopes and half of tin isotopes. We can also see the fission barrier dependence of $\langle E_n \rangle$ around $185 < N < 200$. However, the variations are not large because the mean energies of delayed neutrons do not vary significantly with neutron number.

IV. SUMMARY

In this work, we calculated the BDNE and BDF by combining the discrete β strength function provided by the *pn*-RQRPA [15] and Hauser-Feshbach statistical model [56]. We could improve P_{1n} over a wide range of nuclei as compared with the preceding work of Ref. [15] and obtained the root mean square of P_{1n}, which is comparable to other preceding studies upon adjusting a phenomenological width parameter. The different role of Gaussian- and the Lorentzian-type weight functions was also discussed.

We next discussed partial β-delayed neutron branching ratios P_{xn}. With increasing x, the distribution of P_{xn} approaches the more-neutron-rich side, and the number of nuclei with a prominent P_{xn} significantly decreases. We also studied the variations from the *pn*-RQRPA calculations that use the cutoff method. We concluded that the cutoff method works reasonably well only if $0n$ and $1n$ emissions are the main decay channels, while isotope production ratios calculated by the HFM calculation becomes important to obtain an exact result for neutron-rich nuclei that emits multiple β-delayed neutrons. Calculated β-delayed neutron spectra of ^{89}Br and ^{138}I were compared with the experimental data and it turned out that the *pn*-RQRPA + HFM was able to emulate the experimental data although some fine structures were not reproduced well. We also calculated the β-delayed neutron yield of thermal-neutron-induced fission of ^{235}U. The computed result underestimated the experimental data by about 35%. We pointed out that the discrepancy was due to small P_n of important precursors. An improvement is expected if the P_n of those nuclei are better reproduced.

BDF branching ratios were calculated with four fission barrier data. By comparing the results of the different barrier data, BDF commonly became important around $93 \leqslant Z \leqslant 110$ and $184 \leqslant N \leqslant 200$. It was also found that most nuclei fission directly with a high probability after β decay without emitting neutrons. However, we confirmed that both P_f and P_{xnf} for most nuclei vary greatly over the fission barrier data used. Taking fermium isotopes as an example, we discussed the relation between the BDF branching ratios and barrier heights, and it was found that the BDF are sensitive not only to the barrier height but also to the number of barrier humps. The FRDM results in a single-humped barrier of relatively low height, so that P_f and P_{xnf} are larger than the other fission data, while HFB-14 and ETFSI give a multihumped barrier, so that P_f and P_{xnf} are smaller than the other fission data. However, the number of nuclei given in HFB-14 and ETFSI is smaller than FRDM and SBM. For this reason, it is difficult to choose the best BDF data that can be recommended from our results. However, the products with four barriers allow further sensitive studies of *r*-process nucleosynthesis on the nuclear fission. To accurately assess the role of BDF in the *r* process, detailed information (fission path, curvature, the number of barrier hump, etc.) and an extension to a wide range of nuclei based on microscopic models are highly required.

We also discussed the mean number and energy of delayed neutrons. For most nuclei, the mean number of delayed neutrons is less than 1. As the ratio of neutron number to proton number becomes appreciably large, the mean number of delayed neutrons increases. We also studied the fission barrier dependence and found that the mean number becomes high if BDF is suppressed. The mean number for *pn*-RQRPA + HFM was smaller than that of *pn*-RQRPA because excitation energies were reduced by β-delayed neutrons. The mean energy of delayed neutrons was large for light nuclei and nuclei close to the magic numbers. It was explained that this was governed by the interplay of the level densities of decayed nuclei and the phase space of emitted neutrons. Upon going to neutron-rich nuclei, the mean energy becomes almost constant.

We should comment on several subjects for future work. One of them is level structures of neutron-rich nuclei which were calculated by the phenomenological method as described in Sec. II A because they are not known. More accurate data of BDNE and BDF are expected when the level structures are investigated in the future. We also calculated odd-mass nuclei in the same way as even-mass nuclei, namely, we just imposed the expectation value of the particle number operator to be odd in the RHB calculation. Applying the equal-filling approximation and the blocking approximation, which are more advanced ways to treat odd mass nuclei, may improve the present result. Taking into account continuum states, which become important especially for neutron-rich nuclei, as well as the shape deformation, will also improve the accuracy of BDNE and BDF calculations. Our discussion in this work is limited to neutron-rich nuclei. However, it will be interesting to extend our framework to neutron-deficient nuclei where it is expected that P_α as well as P_p become more important than neutron-rich nuclei.

A table of BDNE, BDF, and β-delayed α-particle emission branching ratios calculated in this work is available in the Supplemental Material [62].

ACKNOWLEDGMENTS

N.P. acknowledges support by the QuantiXLie Centre of Excellence, a project co financed by the Croatian Government and European Union through the European Regional Development Fund and the Competitiveness and Cohesion Operational Programme (KK.01.1.1.01).

[1] E. Burbidge, G. Burbidge, W. Fowler, and F. Hoyle, Rev. Mod. Phys. **29**, 547 (1957).
[2] A. Cameron, Report CRL-41, Chalk River, Ontario (1957).
[3] K. Hotokezaka, P. Beniamini, and T. Piran, Int. J. Mod. Phys. D **27**, 1842005 (2018).
[4] S. Wanajo, Y. Sekiguchi, N. Nishimura, K. Kiuchi, K. Kyutoku, and M. Shibata, Astrophys. J. Lett. **789**, L39 (2014).
[5] C. Freiburghaus, J.-F. Rembges, T. Rauscher *et al.*, Astrophys. J. **516**, 381 (1999).
[6] A. Arcones and G. Martínez-Pinedo, Phys. Rev. C **83**, 045809 (2011).
[7] Q. Zhi, E. Caurier, J. J. Cuenca-García, K. Langanke, G. Martínez-Pinedo, and K. Sieja, Phys. Rev. C **87**, 025803 (2013).
[8] K. Langanke and G. Martínez-Pinedo, Rev. Mod. Phys. **75**, 819 (2003).
[9] J. Beun, J. C. Blackmon, W. R. Hix, G. C. McLaughlin, M. S. Smith, and R. Surman, J. Phys. G **36**, 025201 (2008).
[10] R. Surman, J. Beun, G. C. McLaughlin, and W. R. Hix, Phys. Rev. C **79**, 045809 (2009).
[11] M. R. Mumpower, G. C. McLaughlin, and R. Surman, Phys. Rev. C **86**, 035803 (2012).
[12] Y. Xu, S. Goriely, A. J. Koning, and S. Hilaire, Phys. Rev. C **90**, 024604 (2014).
[13] I. N. Borzov and S. Goriely, Phys. Rev. C **62**, 035501 (2000).
[14] T. Suzuki, T. Yoshida, T. Kajino, and T. Otsuka, Phys. Rev. C **85**, 015802 (2012).
[15] T. Marketin, L. Huther, and G. Martínez-Pinedo, Phys. Rev. C **93**, 025805 (2016).
[16] M. Mumpower, R. Surman, G. McLaughlin, and A. Aprahamian, Prog. Part. Nucl. Phys. **86**, 86 (2016).
[17] N. Nishimura, Z. Podolyák, D.-L. Fang, and T. Suzuki, Phys. Lett. B **756**, 273 (2016).
[18] T. Suzuki, S. Shibagaki, T. Yoshida, T. Kajino, and T. Otsuka, Astrophys. J. Lett. **859**, 133 (2018).
[19] T. Kodama and K. Takahashi, Phys. Lett. B **43**, 167 (1973).
[20] T. Kodama and K. Takahashi, Nucl. Phys. A **239**, 489 (1975).
[21] K.-L. Kratz, F.-K. Thielemann, W. Willebrandt, P. Möller, V. Harms, A. Wohr, and J. W. Truran, J. Phys. G: Nucl. Phys. **14**, S331 (1988).
[22] J. Beun, G. C. McLaughlin, R. Surman, and W. R. Hix, Phys. Rev. C **77**, 035804 (2008).
[23] S. Goriely, Eur. Phys. J. A **51**, 22 (2015).
[24] M. Eichler, A. Arcones, R. Käppeli, O. Korobkin, M. Liebendörfer, G. Martínez-Pinedo, I. V. Panov, T. Rauscher, S. Rosswog, F.-K. Thielemann, and C. Winteler, J. Phys.: Conf. Ser. **665**, 012054 (2016).
[25] S. Shibagaki, T. Kajino, G. J. Mathews, S. Nishimura, S. Chiba, and G. Lorusso, Astrophys. J. Lett. **816**, 79 (2016).
[26] M. R. Mumpower, T. Kawano, T. M. Sprouse *et al.*, Astrophys. J. Lett. **869**, 14 (2018).
[27] S. A. Giuliani, G. Martínez-Pinedo, and L. M. Robledo, Phys. Rev. C **97**, 034323 (2018).
[28] I. Petermann, K. Langanke, G. Martínez-Pinedo *et al.*, Eur. Phys. J. A **48**, 122 (2012).
[29] R. Caballero-Folch, C. Domingo-Pardo, J. Agramunt *et al.*, Phys. Rev. Lett. **117**, 012501 (2016).
[30] K. P. Rykaczewski, JAEA-Conf **2018-001**, 13 (2018).
[31] K. Miernik, K. P. Rykaczewski, R. Grzywacz, C. J. Gross, M. Madurga, D. Miller, D. W. Stracener, J. C. Batchelder, N. T. Brewer, A. Korgul, C. Mazzocchi, A. J. Mendez, II, Y. Liu, S. V. Paulauskas, J. A. Winger, M. Wolińska-Cichocka, and E. F. Zganjar, Phys. Rev. C **97**, 054317 (2018).
[32] J. Agramunt, J. Tain, M. Gómez-Hornillos *et al.*, Nucl. Instrum. Methods Phys. Res., Sect. A **807**, 69 (2016).
[33] R. Dunlop, C. E. Svensson, C. Andreoiu, G. C. Ball, N. Bernier, H. Bidaman, V. Bildstein, M. Bowry, D. S. Cross, I. Dillmann, M. R. Dunlop, F. H. Garcia, A. B. Garnsworthy, P. E. Garrett, G. Hackman, J. Henderson, J. Measures, D. Mucher, B. Olaizola, K. Ortner, J. Park, C. M. Petrache, J. L. Pore, J. K. Smith, D. Southall, M. Ticu, J. Turko, K. Whitmore, and T. Zidar, Phys. Rev. C **99**, 045805 (2019).
[34] From ENSDF database as of Month day, Year (12-Dec-2019), Version available at http://www.nndc.bnl.gov/ensarchivals/.
[35] L. Ghys, A. N. Andreyev, S. Antalic, M. Huyse, and P. Van Duppen, Phys. Rev. C **91**, 044314 (2015).
[36] K.-L. Kratz and G. Herrmann, Eur. Phys. J. A **263**, 435 (1973).
[37] E. A. McCutchan, A. A. Sonzogni, T. D. Johnson, D. Abriola, M. Birch, and B. Singh, Phys. Rev. C **86**, 041305(R) (2012).
[38] K. Miernik, Phys. Rev. C **88**, 041301(R) (2013).

[39] K. Miernik, Phys. Rev. C **90**, 054306 (2014).
[40] A. N. Andreyev, M. Huyse, and P. Van Duppen, Rev. Mod. Phys. **85**, 1541 (2013).
[41] T. Yoshida and T. Tachibana, J. Nucl. Sci. Technol. (Abingdon, U. K.) **37**, 491 (2000).
[42] T. Tachibana, RIKEN Review, Focused on Models and Theories of the Nuclear Mass **26**, 109 (2000).
[43] K. Nomura, R. Rodríguez-Guzmán, and L. M. Robledo, Phys. Rev. C **101**, 044318 (2020).
[44] S. Yoshida, Y. Utsuno, N. Shimizu, and T. Otsuka, Phys. Rev. C **97**, 054321 (2018).
[45] T. Suzuki, S. Shibagaki, T. Yoshida *et al.*, R-process nucleosynthesis in core-collapse supernova explosions and binary neutron star mergers, in *Nuclei in the Cosmos XV*, edited by A. Formicola, M. Junker, L. Gialanella, and G. Imbriani (Springer, Cham, 2019), Vol. 219, p. 437.
[46] A. Staudt and H. Klapdor-Kleingrothaus, Nucl. Phys. A **549**, 254 (1992).
[47] M. Hirsch, A. Staudt, and H. Klapdor-Kleingrothaus, At. Data Nucl. Data Tables **51**, 243 (1992).
[48] P. Möller, J. Nix, and K.-L. Kratz, At. Data Nucl. Data Tables **66**, 131 (1997).
[49] I. N. Borzov, Phys. Rev. C **71**, 065801 (2005).
[50] J.-U. Nabi, N. Çakmak, and Z. Iftikhar, Eur. Phys. J. A **52**, 5 (2016).
[51] I. Panov, Y. Lutostansky, and F.-K. Thielemann, J. Phys.: Conf. Ser. **665**, 012060 (2016).
[52] M. T. Mustonen, T. Shafer, Z. Zenginerler, and J. Engel, Phys. Rev. C **90**, 024308 (2014).
[53] M. T. Mustonen and J. Engel, Phys. Rev. C **93**, 014304 (2016).
[54] E. M. Ney, J. Engel, T. Li, and N. Schunck, Phys. Rev. C **102**, 034326 (2020).
[55] M. R. Mumpower, T. Kawano, and P. Möller, Phys. Rev. C **94**, 064317 (2016).
[56] W. Hauser and H. Feshbach, Phys. Rev. **87**, 366 (1952).
[57] T. Kawano, P. Möller, and W. B. Wilson, Phys. Rev. C **78**, 054601 (2008).
[58] P. Möller, M. Mumpower, T. Kawano, and W. Myers, At. Data Nucl. Data Tables **125**, 1 (2019).
[59] F. K. Thielemann, J. Metzinger, and H. V. Klapdor, Z. Phys. A: At. Nucl. (1975) **309**, 301 (1983).
[60] I. Panov, E. Kolbe, B. Pfeiffer, T. Rauscher, K.-L. Kratz, and F.-K. Thielemann, Nucl. Phys. A **747**, 633 (2005).
[61] F. Minato, EPJ Web Conf. **122**, 10001 (2016).
[62] See Supplemental Material at http://link.aps.org/supplemental/10.1103/PhysRevC.104.044321 for the complete data set containing delayed neutron and fission branching ratios.
[63] T. Marketin, D. Vretenar, and P. Ring, Phys. Rev. C **75**, 024304 (2007).
[64] J. Engel, M. Bender, J. Dobaczewski, W. Nazarewicz, and R. Surman, Phys. Rev. C **60**, 014302 (1999).
[65] P. Ring and P. Schuck, *The Nuclear Many-Body Problem* (Springer-Verlag, Berlin, 1980).
[66] O. Iwamoto, J. Nucl. Sci. Technol. (Abingdon, U. K.) **44**, 687 (2007).
[67] Y. F. Niu, G. Colò, E. Vigezzi, C. L. Bai, and H. Sagawa, Phys. Rev. C **94**, 064328 (2016).
[68] L. W. Nordheim, Phys. Rev. **78**, 294 (1950).
[69] A. Koning and J. Delaroche, Nucl. Phys. A **A713**, 231 (2003).
[70] Avrigeanu, Phys. Rev. C **82**, 014606 (2010).
[71] A. Gilbert and A. G. W. Cameron, Can. J. Phys. **43**, 1446 (1965).
[72] M. A. and Y. Nakajima, J. Nucl. Sci. Technol. (Abingdon, U. K.) **31**, 151 (1994).
[73] J. Kopecky and M. Uhl, Phys. Rev. C **41**, 1941 (1990).
[74] M. Liu, N. Wang, Y. Deng, and X. Wu, Phys. Rev. C **84**, 014333 (2011).
[75] D. L. Hill and J. A. Wheeler, Phys. Rev. **89**, 1102 (1953).
[76] S. Goriely, M. Samyn, and J. M. Pearson, Phys. Rev. C **75**, 064312 (2007).
[77] A. Mamdouh, J. Pearson, M. Rayet, and F. Tondeur, Nucl. Phys. A **679**, 337 (2001).
[78] P. Möller, A. J. Sierk, T. Ichikawa, A. Iwamoto, and M. Mumpower, Phys. Rev. C **91**, 024310 (2015).
[79] H. Koura, Prog. Theor. Exp. Phys. **2014**, 113D02 (2014).
[80] R. Capote, M. Herman, P. Obložinský *et al.*, Nucl. Data Sheets **110**, 3107 (2009).
[81] S. Goriely, S. Hilaire, and A. J. Koning, Phys. Rev. C **78**, 064307 (2008).
[82] P. Dimitriou, I. Dillmann, B. Singh, V. Piksaikin, K. Rykaczewski, J. Tain, A. Algora, K. Banerjee, I. Borzov, D. Cano-Ott, S. Chiba, M. Fallot, D. Foligno, R. Grzywacz, X. Huang, T. Marketin, F. Minato, G. Mukherjee, B. Rasco, A. Sonzogni *et al.*, Nucl. Data Sheets **173**, 144 (2021).
[83] K. Pham, J. Jänecke, D. A. Roberts, M. N. Harakeh, G. P. A. Berg, S. Chang, J. Liu, E. J. Stephenson, B. F. Davis, H. Akimune, and M. Fujiwara, Phys. Rev. C **51**, 526 (1995).
[84] P. Möller, A. Sierk, T. Ichikawa, and H. Sagawa, At. Data Nucl. Data Tables **109-110**, 1 (2016).
[85] J. Katakura, *JENDL FP DD File 2011 and FY File 2011*, Tech. Rep. JAEA-Data/Code 2011-025 (Japan Atomic Energy Agency, 2012).
[86] J. Katakura, F. Minato, and K. Ohgama, EPJ Web Conf. **111**, 08004 (2016).
[87] G. Keepin, T. Wimett, and R. Zeigler, J. Nucl. Energy **6**, 1044 (1957).
[88] P. Schillebeeckx, M. Verwerft, G. Žerovnik, Y. Parthoens, B. Pedersen, G. Alaerts, G. Cools, K. Govers, J. Paepen, G. Varasano, and R. Wynants, A non-destructive method to determine the neutron production rate of a sample of spent nuclear fuel under standard controlled area conditions, JRC Technical Report No. JRC121586 (2020), doi:10.2760/614853.
[89] G. Bentoumi, R. Rogge, F. Ali, L. Li, and B. Sur, Ann. Nucl. Energy **152**, 108001 (2021).
[90] D. Brown, M. Chadwick, R. Capote, A. Kahler, A. Trkov, M. Herman, A. Sonzogni, Y. Danon, A. Carlson, M. Dunn, D. Smith, G. Hale, G. Arbanas, R. Arcilla, C. Bates, B. Beck, B. Becker, F. Brown, R. Casperson, J. Conlin *et al.*, Nucl. Data Sheets **148**, 1 (2018).
[91] G. Rudstam and S. Shalev, Nucl. Phys. A **235**, 397 (1974).
[92] S. Shalev and G. Rudstam, Nucl. Phys. A **230**, 153 (1974).
[93] M. Lewis, Nucl. Data Sheets **5**, 631 (1971).